

**The Impact of Climate Variability on the
Distribution of Radiocarbon in CM2Mc, a New
Earth System Model**

Eric Galbraith
McGill University, Montreal, QC

Anand Gnanadesikan, Stephen Griffies, John Dunne, Andrew Wittenberg,
Isaac Held
Geophysical Fluid Dynamics Laboratory, Princeton, NJ

Eun Young Kwon, Keith Rodgers, Daniele Bianchi, Jorge Sarmiento,
Richard Slater
Princeton University, Princeton, NJ

Jennifer Simeon
Institut Pierre Simon Laplace, Paris, FR

Abstract

The distribution of radiocarbon (^{14}C) in the ocean and atmosphere has fluctuated on timescales ranging from seasons to millennia. It is thought that these fluctuations partly reflect variability in the climate system, offering a rich potential source of information to help understand mechanisms of past climate change. However, ^{14}C has not previously been included as a tracer in coupled ocean-atmosphere models. Here, a long simulation with a new, coupled model is used to explore the mechanisms that redistribute ^{14}C within the Earth system on inter-annual to centennial timescales. The model, CM2Mc, is a lower-resolution version of the Geophysical Fluid Dynamics Laboratory's CM2M model, uses no flux adjustments, and incorporates a simple prognostic ocean biogeochemistry model including radiocarbon. The atmospheric ^{14}C is held constant, so that the oceanic distribution of radiocarbon is only a function of internal climate variability. The simulation reveals robust relationships between sea surface ^{14}C and the model-equivalents of both the El Nino Southern Oscillation and the Southern Annular Mode, and a particularly strong link between the Indonesian Throughflow and the ^{14}C of the eastern Indian Ocean. Radiocarbon variability also illuminates episodic ventilation events in the Southern Ocean, caused by breakdowns of the shallow salinity stratification. Although these events expose radiocarbon-depleted waters at the surface, the accompanying variability in air-sea exchange is too small to have contributed significantly to the atmospheric radiocarbon variability of the past millennium, consistent with prior evidence that changes in the rate of radiocarbon production dominated atmospheric variability over this interval.

1. Introduction

One of the great challenges in understanding the ocean's role in climate variability is the scarcity of direct measurements, particularly prior to the last few decades. Such data limitations seriously hinder progress in understanding modes of inter-annual variability. These modes include the El Niño Southern Oscillation (ENSO), for which continuous observations of many centuries are required for accurate characterization (Wittenberg, 2009; Vecchi and Wittenberg, 2010), and changes in the Southern Ocean overturning and Southern Annular Mode (SAM), which vary on timescales of multiple decades (Visbeck, 2009). Proxy data can help to fill this gap, but many proxy measurements are confounded by spurious influences and are difficult to interpret.

Radiocarbon is one such proxy, directly recorded with high fidelity by marine micro-plankton providing decadal-centennial resolution (Hughen et al., 1998), and in both corals and tree rings at annual or even subannual resolution. Thousands of individual tree-ring records have been spliced together to reconstruct the radiocarbon history of the troposphere in both the northern and southern hemispheres (Figure 1). Meanwhile, long coral records of radiocarbon have been recovered from the tropics (Druffel, 1997; Guilderson et al., 1998; Druffel et al., 2004; Fallon and Guilderson, 2008; Guilderson et al., 2009), revealing inter-annual variability in local seawater radiocarbon well in excess of the analytical error associated with coral measurements (~ 3 ‰ measurement error, Guilderson et al., 2009). Looking even further back in time, large changes in the radiocarbon activities of the ocean and atmosphere accompanied the warming that occurred at the end of the last ice age (Shackleton et al., 1988; Hughen et al., 1998; Galbraith et al., 2007; Marchitto et al., 2007; Skinner et al., 2010). Unfortunately, the

manifold influences on radiocarbon activities can confuse the translation of these geochemical archives to useful climate information.

Radiocarbon is produced in the stratosphere and upper troposphere by cosmic rays, at a rate dependent on the strengths of the geomagnetic field and the solar wind (Masarik and Beer, 1999), and decays with a 5730-year half-life. The residence time of radiocarbon in the atmosphere is about 5 years (Muscheler et al., 2007), causing it to be quite well mixed, with only a small interhemispheric gradient (Figure 1). A small portion of radiocarbon is lost through decay in the terrestrial biosphere, while the majority dissolves in the ocean, at a rate dependent on ocean circulation (Siegenthaler et al., 1980). The fact that ^{14}C production takes place exclusively in the atmosphere, coupled with the long air-sea equilibration timescale of carbon, caused the ocean to be everywhere undersaturated with ^{14}C under pre-industrial conditions, but to varying degrees. The slow pace of deep ocean circulation allows radiogenic decay to significantly deplete the ^{14}C activity of abyssal waters, so that strong undersaturation of ^{14}C is a clear tracer of these “old” waters where they come to the surface (Toggweiler et al., 1991; Toggweiler and Samuels, 1993; Rodgers et al., 2000; Gnanadesikan et al., 2004).

The complexity of interpreting radiocarbon arises from the fact that both its natural rate of production, and its distribution within the Earth system, could have changed simultaneously. Variability in the relatively small atmospheric ^{14}C reservoir over the last millennium (Figure 1), including ‘Suess wiggles’ with a characteristic timescale of ~200 y (Suess, 1968), are frequently argued to reflect changes in the production rate of radiocarbon (Siegenthaler et al., 1980; Stuiver and Quay, 1980; Masarik and Beer, 1999; Muscheler et al., 2007). At the same time, interannual modes of climate variability are

thought to drive redistribution of radiocarbon within the ocean (Rodgers et al., 1997; Rodgers et al., 2004; Druffel et al., 2007), with some impact on air-sea exchange. Meanwhile, sustained changes in ocean circulation, such as those thought to have occurred during the end of the last age, are argued to have caused very large changes in the redistribution of radiocarbon between the ocean and atmosphere (Siegenthaler et al., 1980; Hughen et al., 1998; Broecker and Barker, 2007). These processes have been variously explored with box models (Siegenthaler et al., 1980) and GCMs (Toggweiler et al., 1989; Toggweiler et al., 1991; Rodgers et al., 1997), and radiocarbon has proven a useful diagnostic of the mean ocean circulation (Duffy et al., 1997; Guilderson et al., 2000; Gnanadesikan et al., 2004; Matsumoto et al., 2004; Grunet et al., 2005). However, the relationship between climate variability and the global distribution of natural radiocarbon on centennial timescales has received little attention.

In this paper we examine how oceanic radiocarbon is linked to natural, unforced variability in a free-running global coupled climate model with no flux adjustments, but with a fixed atmospheric radiocarbon activity. To our knowledge, this is the first time radiocarbon has been included as a tracer in a coupled ocean-atmosphere model. The newly-developed model is of relatively coarse resolution, enabling us to simulate hundreds of years with many different tracers using reasonable computational resources, but is still relatively realistic, displaying robust modes of unforced ocean-atmosphere variability on decadal timescales. Section 2 describes the formulation of the model. Section 3 presents the climate simulation produced under pre-industrial radiative forcing, with comparisons to the observational record. Section 4 examines the relationship between modes of climate variability and oceanic radiocarbon within the model, and

section 5 discusses how ocean circulation modulates the air-sea balance of radiocarbon.

Section 6 concludes the paper.

2. Model

The Coupled Model 2 with MOM4p1 at Coarse-resolution (CM2Mc) is similar to the Geophysical Fluid Dynamics Laboratory (GFDL) 1-degree coupled model, CM2.1 (Delworth et al., 2006), used in the Intergovernmental Panel on Climate Change's Fourth Assessment Report. However, the resolution of both the atmospheric and oceanic grids has been coarsened in order to decrease computational cost, and the model uses an updated version of the GFDL code, prepared in anticipation of a suite of simulations for the IPCC Fifth Assessment Report. This updated code includes the ocean model MOM4p1 (Griffies, 2009), which includes a number of numerical and physical improvements, as well as the option of using pressure for the vertical co-ordinate instead of depth, so that steric sea level is directly simulated. Modifications made to the CM2.1 atmosphere are minor, involving a reduction of spatial resolution and minimal parameter changes. More substantial changes were made to the ocean component, including improvements to the subgrid-scale parameterizations of ocean mixing, of critical importance to low-resolution climate models incapable of capturing processes such as mesoscale eddies and gravity-driven bottom flows. CM2Mc requires approximately one tenth the computational cost of the higher resolution model. Additional model configuration details and diagnostics can be found on the website <http://sites.google.com/site/cm2cmodel/>.

139 *a) Atmospheric model configuration*

140 The atmosphere is very similar to the GFDL Atmospheric Model 2 (AM2), as described
141 by the GFDL Global Atmospheric Model Development Team (Anderson et al., 2004), but
142 using the finite volume dynamical core of Lin (2004), as implemented in CM2.1
143 (Delworth et al., 2006). The atmosphere used here employs the M30 grid, with a
144 latitudinal resolution of 3 degrees and a longitudinal resolution of 3.75 degrees, instead of
145 the M45 grid used in CM2.1 (2 degrees by 2.5 degrees), but uses the same vertical
146 configuration with 24 levels. The decreased horizontal resolution results in 44% of the
147 number of grid cells in the CM2.1 atmosphere, a relatively modest decrease in resolution.
148 However, the atmospheric time steps are also increased, from 0.5 to 1.5 hours for the
149 tracer time step, from 6 to 9 minutes for the dynamical timestep, and from 2 to 3 hours
150 for the radiative time step.

151 The change in discretization required a small readjustment of two cloud
152 parameters in order to maintain a net radiation balance close to zero under modern
153 climate, which had negligible impact on atmospheric dynamics. In addition, the mountain
154 gravity drag parameter G^* (Anderson et al., 2004) was decreased from 1.0 to 0.5 in order
155 to compensate for the coarser horizontal resolution. The final alteration was the
156 replacement of the sea salt aerosol climatology of Haywood et al. (1999), used for the
157 radiative conditions, with a more recent estimate from Ginoux (2006). As in CM2.1, the
158 Land Dynamics model of Milly and Shmakin (2002) is used, including a river routing
159 scheme but no terrestrial ecosystem (see Anderson et al. (2004)).

b) Ocean grid and bathymetry

The CM2Mc ocean uses a tripolar grid (Murray, 1996) to avoid the grid singularity at the north pole, as in GFDL's CM2.0 and CM2.1 models (Griffies et al., 2005; Gnanadesikan et al., 2006). The horizontal dimensions of the ocean grid vary according to latitude, with the finest latitudinal resolution at the equator is 0.6 degrees, allowing an explicit physical representation of the equatorial currents. There are 28 vertical levels, the uppermost eight of which are each 10 dbar thick, below which the levels gradually increase in thickness to a maximum of 506 dbar. The model employs partial bottom cells (Adcroft et al., 1997; Pacanowski and Gnanadesikan, 1998) to allow a more realistic representation of the bathymetry.

The bathymetry was initially generated from averaging of satellite-derived bathymetry onto the coarser model grid, with a smoothing algorithm. The result was then carefully examined, and critical features destroyed in the regridding process were manually restored. In order to compensate for mixing between ocean basins and marginal seas where the coarse resolution of the topography does not resolve the narrow connections, the cross-land mixing scheme of Griffies et al. (2005) is employed, generating less than 2 Sv of total mixing at each of six locations. Finally, where the discharge locations for precipitation falling on Antarctica led to the margins of the Ross or Ronne-Filchner ice shelves, they were shifted north of the coast by a few degrees, in order to roughly account for the transport of freshwater by drifting icebergs.

c) Ocean model parameterizations

CM2Mc uses the MOM4p1 code with pressure as the vertical coordinate thus allowing the model to solve the non-Boussinesq primitive equations. The vertically integrated

mode is time-stepped using an explicit bottom pressure solver, and the transfer of water mass across the ocean surface occurs using real freshwater fluxes. Tracer advection uses the MDPPM scheme for temperature and salinity (Adcroft et al., 2004), and the Sweby MDPL scheme for other tracers (Griffies et al., 2005). Light is absorbed by water and a chlorophyll field following the Manizza et al. (2005) algorithm. Over the initial millennium of simulation a smoothly-varying, satellite-derived climatological chlorophyll field was used, after which the chlorophyll concentrations used for shortwave absorption were those predicted by a coupled biogeochemical model (BLING, described by Galbraith et al. (2010), not shown here). The gross metrics of the simulation did not change significantly with the change to prognostic chlorophyll.

Most subgridscale parameterizations for mixing are similar to those used in the CM2 series (Griffies et al., 2005). The lateral friction uses an isotropic Smagorinsky viscosity in mid-latitudes, while within 20 degrees of the equator the anisotropic NCAR viscosity is used. Lateral diffusion and skew diffusion of tracers along isopycnals is represented using the parameterization of Gent and McWilliams (1990) with a spatially varying diffusion coefficient, A_{GM} , as determined in CM2.1 (Griffies et al., 2005). The space and time scale in this coefficient depends on the horizontal shear between 100 m and 2000 m. A minimum coefficient of $200 \text{ m}^2/\text{s}$ and a maximum coefficient of $1400 \text{ m}^2/\text{s}$ are imposed. The slope-dependent thickness transport also stops increasing at a value of $A_{GM} * S_{\text{max}}$, where the maximum isopycnal slope S_{max} is set to 0.01, whereas it is set to 0.002 in CM2.1 (see Gnanadesikan et al. (2007) and Farnetti et al. (2010) for discussions of this parameter). Overall, these changes generate a more active eddy mixing parameterization than CM2.1, with a greater responsiveness to changes in baroclinicity,

as suggested by recent observations in the Southern Ocean (Boning et al., 2008).

Meanwhile, the neutral diffusion coefficient for tracers, A_I , is set to a constant value of $800 \text{ m}^2/\text{s}$.

Within the boundary layer, we use the K-profile parameterization of Large et al., (1994). Away from the boundary layer, a background diffusivity of $0.1 \times 10^{-4} \text{ m}^2 \text{ s}^{-1}$ and a background viscosity of $1 \times 10^{-4} \text{ m}^2 \text{ s}^{-1}$ are used. Below 300 m, these background coefficients are punctuated by locally intense vertical mixing, as shown by tracer studies (Naveira Garabato et al., 2004), where gravity waves are generated over regions of rough topography and break as they propagate upward into the water column. This process is parameterized with the tidally-dependent mixing scheme of Simmons et al. (2004), that depends on the local stratification as well as prescribed bottom roughness and tidal amplitude. In addition, tidal mixing in coastal areas is simulated by the mixing scheme of Lee et al. (2006) which adds turbulence generated by tidal currents in the turbulent bottom boundary layer to the KPP scheme.

d) Marine Biogeochemical model

We use a new idealized ocean biogeochemistry (iBGC) model in order to simulate radiocarbon distributions, based on simple representations of nutrient uptake and remineralization. The effect of organic matter cycling on the radiocarbon distribution is small, but we describe the model briefly here for completeness.

Conceptually, this model is very similar to the pioneering biogeochemical model of Bacastow and Maier-Reimer (1990). In brief, it carries a single prognostic inorganic macronutrient tracer which we call phosphate (PO_4), and represents the net activity of phytoplankton through an uptake function in all ocean grid cells as a function of

temperature, T and available light, I . Once taken up, the macronutrient is instantaneously partitioned between a dissolved organic phosphorus (DOP) tracer and a flux of sinking particulate organic phosphorus (POP), according to a fixed fraction, ϕ . The sinking of POP is not achieved by using a prognostic tracer but, instead, by instantaneously redistributing remineralized PO_4 throughout the water column beneath the layer in which uptake occurred, similar to the OCMIP2 scheme (Najjar and Orr, 1998). Meanwhile, DOP decays to PO_4 according to a temperature-dependent first-order rate, $\gamma = \gamma_0 e^{k_r T}$, where k_r gives the temperature-dependency of remineralization and T is temperature (degrees C). The total mass of phosphorus ($PO_4 + DOP$) is conserved within the ocean. The overall equation for PO_4 is

$$\frac{dPO_4}{dt} = Circ(PO_4) - V_{max} e^{kT} (1 - e^{-I/I_k}) \frac{PO_4}{kPO_4 + PO_4} + \gamma DOP + remi_{pop} \quad (1)$$

where $Circ$ indicates the net effect of ocean advection and mixing, V_{max} is the maximum uptake rate, k is a constant determining the temperature sensitivity of uptake, I_k is a constant determining the tendency for light limitation, $remi_{POP}$ is the remineralization source of phosphorus from sinking POP, and kPO_4 is a constant determining the tendency for nutrient limitation.

Dissolved inorganic carbon (DIC) is carried as a prognostic tracer, with air-sea gas exchange following the OCMIP2 protocol (Najjar and Orr, 1998) and the Wanninkhof (1992) windspeed-dependent piston velocity, using salinity to estimate alkalinity (*i.e.* with no carbonate cycling). Organic carbon, dissolved and particulate, is not carried as an explicit tracer, but is assumed to be linked to the cycling of organic phosphorus through a strict stoichiometric ratio of 106 C:P (Redfield et al., 1963).

Dissolved inorganic radiocarbon ($DI^{14}C$) is also carried as a prognostic tracer, with a

concentration equal to its true concentration divided by the pre-bomb atmospheric $^{14}\text{C}/^{12}\text{C}$ ratio, so that the concentrations are numerically similar to those of DIC. DI^{14}C undergoes the same air-sea exchange processes as DIC but, in contrast to total carbon, its cycling also includes uptake by plankton and export as particulate organic ^{14}C , as well as partitioning of uptake into a dissolved organic ^{14}C tracer, DO^{14}C . The $\Delta^{14}\text{C}$ (see Stuiver and Polach (1977) for the definition of this quantity) in equilibrium with the atmosphere is prescribed (equal to 0‰ in the simulations shown here), and the half-life for decay is 5730 y. All parameters used in iBGC are given in Table 1.

3. Model simulation

a) Atmosphere-only simulation

As a preliminary test, the atmospheric model was integrated for twenty years with prescribed SST and constant '1990' radiative conditions, following the AMIP method described by Anderson et al. (2004). In general, this simulation shows a very similar pattern of biases to the 2-degree configuration of the atmosphere, with slightly greater errors for all variables. The radiative balance of the atmosphere-only model was $+0.45 \text{ W m}^{-2}$; with pre-industrial radiative conditions and modern SST, the radiative balance was -1.67 W m^{-2} .

b) Coupled simulation

When coupled to the ocean model, the atmospheric simulation exhibits some pronounced differences in comparison to the prescribed-SST run, generally consistent with the effect

of coupling the 2-degree M45 atmosphere to the 1-degree ocean of CM2.1 (Delworth et al., 2006; Wittenberg et al., 2006). Key differences include the appearance of a ‘split’ Inter-Tropical Convergence Zone (ITCZ), *i.e.* excessive rainfall in the Pacific just south of the equator (Figure 2), and an increase in the excess heating above eastern boundary upwelling regions and the Southern Ocean (Figure 2).

When forced with pre-industrial radiative conditions, the global energy balance of the coupled model is significantly more positive than in the prescribed-SST case. The net radiation imbalance quickly rises as the ocean surface adjusts, stabilizing at $+0.68 \text{ W m}^{-2}$ over the latter half of the first century, then gradually declines as the deep ocean warms, reaching $\sim 0.4 \text{ W m}^{-2}$ by the end of the simulation (approximately 2000 years). Note that the atmospheric model does not conserve energy perfectly, consistently leaking $\sim 0.4 \text{ W m}^{-2}$ due to the fact that, unlike the ocean and land models, the atmosphere does not account for the heat content of water (Delworth et al., 2006). A timeseries of ocean temperature shows that the model is very close to thermal balance at the end of the simulation (not shown).

The most significant temperature and salinity errors of the ocean simulation (Figure 3) can be directly attributed to the errors of the atmospheric simulation. Foremost among these are: 1) a cold bias in the North Pacific, particularly during boreal summer; 2) a warm bias in the Southern Ocean, particularly during austral summer; 3) warm biases in all eastern boundary upwelling regions; 4) a low salinity bias in the South Pacific and high salinity bias in the North Pacific (compare Figures 2 and 3). The first, second and third errors can be attributed to the regional energy balances, apparently due to inaccuracies in the representation of clouds that produce very similar errors in absorbed

shortwave radiation in both the prescribed-SST and coupled simulations. Meanwhile, the fourth, a result of the split ITCZ, arises from the coupling between the ocean and atmosphere in the tropical Pacific, and is a common symptom of coupled models (De Szoeké and Xie, 2008). The warm bias of the Southern Ocean, combined with a tendency for North Atlantic Deep Water to originate as excessively warm and salty, leads to a globally-warm bias of the whole ocean in situ temperature, 4.6°C (vs. 4.3°C for CM2.1 and 3.0°C for observations, Conkright et al., 2002). Gross metrics of the ocean simulation are given in Table 2.

Compared to CM2.1, the overturning circulation is significantly different, most importantly in the circulation of deep waters formed in the Southern Ocean. CM2.1 ventilates a continuous water column throughout the Weddell Sea, evident in the ideal age and salinity sections (See Figure 7 of Gnanadesikan et al. (2006)) and in disagreement with observations. In contrast, CM2Mc ventilates at a lower rate, closer to the Antarctic continent, evident in the overturning cell at $\sigma_2 \sim 1037$ (compare Figure 4, top right, of this paper with Figure 6d of Gnanadesikan et al., 2006). Despite the lower ventilation rate, the bottom waters produced by CM2Mc circulate more vigorously throughout the global abyss (compare Figure 4, top panels, with Figures 6c,d of Gnanadesikan et al. (2006)) consistent with observations, such as the strong bottom water flows recently observed near the Kerguelen Plateau (Fukamachi et al., 2010). The contrast in Southern Ocean ventilation appears to be due to a combination of the eddy parameterization (which enhances the eddy flux to high latitudes in CM2Mc, thereby abetting deep sinking), the altered freshwater discharge map (which allows higher

nearshore salinities in CM2Mc), and the model grid. The supply of NADW to the deep ocean is very similar between the two models.

(d) Marine biogeochemical simulation

The marine biogeochemical tracers were integrated synchronously with the physical simulation for the latter half of the run (approximately 1000 years). The description in this section pertains to the final 100 years of this run, while the following section discusses variability during the latter 500 years of the run.

The simulated PO_4 field is fairly close to observations, especially considering the simplicity of the biogeochemical model and errors in the simulated ocean circulation. The principal features of the surface PO_4 field are well captured (Figure 5), including the very elevated Southern Ocean concentrations, low oligotrophic gyre concentrations, and elevated concentrations in low latitude upwelling regions. We note that the high nutrient surface regions occur in the absence of explicit iron limitation.

The largest discrepancy versus observations occurs in the North Pacific, where the surface nutrient concentration is dramatically lower than observed. This can be attributed to errors in the physical ocean circulation, related to the cold atmospheric bias: weak stratification at shallow to mid-depths in the North Pacific causes the circulation to be only weakly estuarine, so that ‘nutrient trapping’ within the basin is much less effective than in reality, leading to erroneously low intermediate-depth nutrient concentrations (Figure 5). In contrast, the Atlantic meridional section shows PO_4 concentrations that are close to the observations (Figure 5).

The sea surface radiocarbon simulation is more difficult to evaluate, given that almost all available observations were made after massive contamination of surface

waters by above-ground nuclear weapons testing in the 1950s and early 1960s. Chemistry-based regression estimates of the pre-bomb radiocarbon activities are available (Rubin and Key, 2002), but these are less reliable in surface waters, and do not correct for the invasion of ^{14}C -depleted emissions from fossil-fuel burning (Suess, 1953). A comparison of the model simulation to the GLODAP regression-based product shows similar large-scale surface $\Delta^{14}\text{C}$ patterns, with simulated $\Delta^{14}\text{C}$ values generally higher in the model. The higher model $\Delta^{14}\text{C}$ is partly attributable to the lack of correction for fossil-fuel carbon, but may also reflect air-sea exchange errors. At the same time, the $\Delta^{14}\text{C}$ in tropical upwelling regions is lower than expected from the coral-based preindustrial estimates summarized in Toggweiler (1993), which could suggest excessive vertical mixing across the tropical thermocline.

The distribution of radiocarbon in the ocean interior, isolated from the fossil fuel effect, agrees better with estimates of natural radiocarbon, but confirms the circulation-error biases as apparent from the phosphate simulation: in the Atlantic, the water mass structure is well reproduced, while in the Pacific, weak stratification of the mid-depth ocean also allows excessive ventilation from above (Figure 6). Both the overactive North Pacific ventilation and the excessive vertical mixing across the thermocline would contribute to the general overestimate of radiocarbon activities in the deep Pacific Ocean.

4. Climate modes and radiocarbon variability

The $\Delta^{14}\text{C}$ of surface seawater shows considerable interannual variability in some regions, as shown in Figure 7 (top left), with complex patterns of correlation to the globally-averaged SST (Figure 7, top right). The interannual variability is most dramatic south of

60°S, where large fluctuations are roughly anti-correlated with SST changes on inter-annual to multi-decadal timescales (Figure 7, bottom right), while the equatorial oceans show pronounced localized correlations and anti-correlations with SST on shorter timescales (Figure 7, bottom left). Here we focus on the dominant climate modes in these two regions, the ENSO and the SAM, to examine the degrees to which these well-known climate modes can explain interannual variability of simulated sea surface $\Delta^{14}\text{C}$. We do this by regressing the deseasonalized monthly anomaly of $\Delta^{14}\text{C}$ onto a climate index representing each mode, using the last 100 years of model output. Statistical significance is tested using a t-test where the effective sample size is estimated by

$$N_{eff} = N \sqrt{\frac{1 - \rho_1 \rho_2}{1 + \rho_1 \rho_2}} \quad (2)$$

(Bretherton et al., 1999) in which N is the length of the time series (in months) and ρ_1 and ρ_2 are the auto-correlation coefficients of $\Delta^{14}\text{C}$ anomaly and the climate index, respectively. The resulting correlation coefficients are only considered if significant at the 99% level.

a) ENSO and radiocarbon

The SST anomaly in the NINO3 region (Figure 8, top left), has an annual peak that is somewhat larger than observed, while the interannual peak is roughly the right size but shifted towards slightly lower frequency. This small degree of disagreement between ~50 years of data and 500 years of model output may not be significant, given the pronounced heterogeneity of ENSO over interdecadal and centennial timescales in models and, presumably, the real world (Wittenberg, 2009). The structure of the warm anomaly is also

very similar to observations (Figure 8, top right) with a correlation coefficient of 0.92, though the zero line is shifted to the west slightly. The wind stress anomaly (Figure 8, bottom left) resulting from this temperature anomaly has about the right magnitude but is also shifted to the west while the wind stress curl anomaly is also about the right magnitude though shifted slightly to the north. In addition, the lagged regression of global SST monthly anomalies onto the NINO3 index is structurally very similar between the model and observations (the first and second columns of Figure 9). Together, these results suggest that the unforced model ENSO variability is operating via similar large-scale mechanisms to those underlying true ENSO variability, and is therefore a suitable tool for studying the effect of ENSO on radiocarbon distributions.

The third column of Figure 9 shows the regression coefficients of the monthly $\Delta^{14}\text{C}$ anomaly versus the NINO3 SST anomaly. The El Niño phase of ENSO, characterized by a high NINO3 SST anomaly (Figure 9, zero lag), is well correlated with positive anomalies of surface $\Delta^{14}\text{C}$ in the western equatorial Pacific Ocean. The correlation arises from a weakening of the easterly winds during El Niño events, which reduces the upwelling of ^{14}C -depleted subsurface waters in the central and eastern equatorial Pacific (Toggweiler et al., 1991). Consequently, the western pool of ^{14}C -enriched surface waters intensifies and expands eastward, resulting in a net accumulation of high- $\Delta^{14}\text{C}$ waters in the western and central equatorial Pacific Ocean.

Meanwhile, the transport of Pacific waters across the Indonesian Through-Flow (ITF) has a large impact on the surface $\Delta^{14}\text{C}$ of the eastern Indian Ocean. A large part of the ITF variability is related to reduced transport during El Niño events (~ 10 Sv, rather than ~ 14 Sv) which restricts the supply of ^{14}C -rich waters from the Pacific warm pool,

and results in the negative correlation shown in Figure 9 for the eastern Indian Ocean (right column). Reduced ITF transport during El Nino events has also been well-documented by observations (Tillinger and Gordon, 2009), but the ITF responds to more than just ENSO, and the $\Delta^{14}\text{C}$ of the eastern Indian Ocean also reflects these additional sources of variability. Illustrating this, the linear correlation of $\Delta^{14}\text{C}$ near the Lombok Strait (11°S, 115°W) with the volume transport of the ITF itself is stronger ($r=0.69$) than it is with the NINO3 SST ($r=0.55$). The slope of the linear regression is $\sim 2 \text{ ‰ Sv}^{-1}$.

The response pattern of $\Delta^{14}\text{C}$ to ENSO is different from that of SST to ENSO in two distinctive ways (Figure 9, compare middle and right columns). While the SST response is characterized by an out of phase relationship between the tropical and extratropical Pacific, the $\Delta^{14}\text{C}$ response is dominated by the zonal contrast between the tropical Pacific and Indian Oceans, resulting from the change in the strength of the Indonesian Throughflow. In addition, the $\Delta^{14}\text{C}$ response persists with very little alteration at a 6-month lag, unlike the SST signal which has largely decayed by this point. This persistence reflects the long air-sea equilibration time of $\Delta^{14}\text{C}$ in seawater (O 10 y), allowing it to maintain a more distinct memory of ocean circulation changes: in effect, the ENSO signal persists throughout an entire year, providing ample opportunity for it to be recorded in corals (Druffel, 1997).

b) SAM and radiocarbon

The Southern Annular Mode (SAM) is a dominant mode of climate variability over the Southern Ocean on interannual to decadal timescales. The SAM is characterized by meridional fluctuations of air masses south of 20°S, associated with changes in sea level

pressure and the location and intensity of the Southern Hemisphere westerlies (e.g. (Hall and Visbeck, 2002; Marshall, 2002). Figure 10 shows the first Empirical Orthogonal Function (EOF) of the monthly sea level pressure anomaly south of 20°S as obtained from the model and observations. In both model and observations, the leading EOF accounts for the major fractions of total variance of sea level pressure with explained variances of 48% and 41%, respectively. The model captures the gross features of the observed leading EOF pattern with a correlation coefficient of 0.96. As with ENSO, this strong similarity between model and observations suggests that the simulated interannual variability is operating via similar mechanisms.

Figure 11 presents the regression coefficients of the monthly anomaly of surface $\Delta^{14}\text{C}$ against the SAM index. The positive SAM correlates well with negative anomalies of $\Delta^{14}\text{C}$ in the Pacific sector of the Southern Ocean, which can be attributed to a strengthening of the westerlies during the positive phase of the SAM, inducing northward Ekman transport and bringing more ^{14}C -depleted water from south of the ACC to the north. However, in spite of the significant correlations between the SAM and $\Delta^{14}\text{C}$ in the Southern Ocean, the SAM is not a dominant driver of $\Delta^{14}\text{C}$ variability in the model. An EOF analysis, using the monthly anomaly of $\Delta^{14}\text{C}$ south of 40°S, shows that the principal component correlated with the SAM index accounts for less than 1% of the total variance of $\Delta^{14}\text{C}$ variability. Instead, the leading mode of $\Delta^{14}\text{C}$ variability south of 40°S, explaining about 61% of the total variance, turns out to be a slowly varying and localized fluctuation, most clearly manifested in the Weddell Sea.

453 *c.) Episodic convection and radiocarbon*

454 The largest surface $\Delta^{14}\text{C}$ variability is centered in the Weddell Sea and is the result of
 455 periodic convective events that exhume ^{14}C -depleted waters from the deep sea; similar
 456 nodes of variability occur in the Ross Sea, as well as the Indian sector of the Southern
 457 Ocean. These events drive the rough anti-correlation of SST and surface $\Delta^{14}\text{C}$ noted
 458 above (Figure 7) and arise from changes in the stratification of the upper water column. It
 459 is entirely possible that this mode of convection is an artifact of the coarse model
 460 resolution, particularly the lack of dense water production on shelves (Toggweiler et al.,
 461 2006); nonetheless, they have a large impact on the modeled air-sea exchange of
 462 radiocarbon, and we therefore discuss them in some detail.

463 Examination of the average annual-mean temperature stratification in the
 464 Weddell Sea (Figure 12a) shows that, whereas surface temperatures are higher during
 465 surface ^{14}C -depletion events, the waters at 300 m are actually slightly colder during
 466 convection, as wintertime cooling stirs cold water to depth. The high surface
 467 temperatures occur because convection brings up enough warm Upper Circumpolar Deep
 468 Water during the wintertime to maintain an ice-free polynya, facilitating more absorption
 469 of solar radiation and much warmer springtime temperatures. Since these changes result
 470 in increased stratification, they cannot by themselves explain the increase in convection.

471 Instead, the cause is a breakdown in the salinity stratification, with convection
 472 occurring when surface salinities approach those of the waters below (Figure 12b). As
 473 shown by the red symbols in Figure 12b, the surface salinity anomalies in the central
 474 Weddell are preceded by salinity anomalies along the prime meridian. We can use times
 475 when there is an anomalous decrease in surface radiocarbon (beyond one standard

deviation) to detect convective onset and times when there is an anomalous increase in surface radiocarbon to detect convective shutoff. As shown in Figure 12c, five years before the onset of convection, salinities are lower than average to the west of the Antarctic Peninsula and higher east of 40W. At the time of convective onset (Figure 12d), the saline anomaly has strengthened and propagated into the central gyre. The anomaly gets even larger at the height of convective activity (Figure 12e). Finally, as fresher water is advected from the east along the southern flank of the gyre, the saline anomaly dwindles and the convection shuts off (Figure 12f).

5. Ocean-driven changes in atmospheric radiocarbon

The radiocarbon variability discussed above is caused by redistributions of radiocarbon within the ocean, due to changes in mixing and advection associated with major climate modes. However, oceanic radiocarbon can also be altered by changes in the air-sea balance of radiocarbon. Although we do not explicitly model atmospheric ^{14}C here, we can infer its general behaviour by analyzing variability in air-sea fluxes.

For this purpose we use the concept of a ‘disequilibrium ^{14}C flux’. This construct, discussed in further detail by Rodgers et al. (submitted) renormalizes the air-sea flux of ^{14}C relative to that of ^{12}C , to avoid the unwieldy fact that their concentrations differ by approximately twelve orders of magnitude. The disequilibrium flux is defined as

$$\phi_{diseq} = \phi_{^{14}\text{C}} r^{12/14} - \phi_{^{12}\text{C}} \quad (2)$$

where $\phi_{^{14}\text{C}}$ is the air-sea ^{14}C flux, $r^{12/14}$ is the pre-bomb atmospheric $^{12}\text{C}/^{14}\text{C}$ ratio (i.e. the ratio preceding contamination by above-ground nuclear weapon testing), and $\phi_{^{12}\text{C}}$ is the

air-sea ^{12}C flux. The results are converted to annual mass fluxes (Pg C a^{-1}). In these units, an instantaneous disequilibrium flux of 1 Pg C would have altered the pre-bomb atmospheric $\Delta^{14}\text{C}$ by approximately $1 \text{ Pg} / M_a$, where M_a is the total mass of atmospheric C ($\sim 700\text{Pg}$), a perturbation of about 1.5%. Note that, by altering the atmospheric ^{14}C inventory, the disequilibrium flux itself would change over time – even given a constant surface $\Delta^{14}\text{C}$ distribution, such that a sustained disequilibrium flux would have a proportionally much smaller effect.

Figure 13 shows the variability in the annually- and zonally-averaged disequilibrium flux, compared to the variability of surface $\Delta^{14}\text{C}$. The surface $\Delta^{14}\text{C}$ variability is large in the high latitudes of both hemispheres, particularly in the south. Meanwhile, the disequilibrium flux shows a different latitudinal distribution, with little variability outside of the Southern Ocean, where the peak is offset from the variability in surface $\Delta^{14}\text{C}$. This contrast arises from the additional importance of wind speed and mixed layer depth in determining the air-sea flux. The dominance of the Southern Ocean occurs because the low ^{14}C content of Upper Circumpolar Deep Water, when exposed at the surface, drives a very large flux of ^{14}C into the ocean relative to ^{12}C . Conversely, when the halocline strengthens and deep ventilation is impeded, surface waters become more radiocarbon-enriched and the uptake of ^{14}C is reduced. As a result, fluctuations in the Southern Ocean circulation have a great deal of leverage in driving the air-sea balance of ^{14}C .

However, when the cumulative air-sea disequilibrium flux is considered over time, even these large fluctuations in the Southern Ocean have a relatively small impact on the resultant atmospheric $\Delta^{14}\text{C}$. We estimate the expected atmospheric response by removing

the detrended average flux of ϕ_{diseq} into the ocean, which essentially balances the decay of radiocarbon within the global ocean, integrating the residual and dividing by M_a (as described above) in order to estimate the oceanic contribution to atmospheric variability with respect to the mean. Note that this calculation will overestimate changes in atmospheric $\Delta^{14}\text{C}$ since, over time, changes driven by the Southern Ocean will equilibrate with the rest of the ocean and terrestrial biosphere. Figure 14 shows the prediction of atmospheric $\Delta^{14}\text{C}$ variability that results from this calculation, over the last 400y of unforced variability in the model. Comparison to Figure 1 clearly shows that the magnitude of atmospheric $\Delta^{14}\text{C}$ variability estimated from model ϕ_{diseq} is much smaller than that reconstructed from tree-ring records of atmospheric $\Delta^{14}\text{C}$: the Southern Ocean circulation changes simulated here, though dramatic, contribute less than +/- 2 ‰ of atmospheric $\Delta^{14}\text{C}$, an order of magnitude smaller than the reconstructed changes.

Two possible, non-exclusive conclusions could be drawn from the small amplitude of the simulated variability. The first possibility is that, despite the apparent fidelity of the ENSO and SAM simulations, the unforced variability in the model is significantly smaller than that of the real world on multi-decadal timescales. Indeed, the lack of variability in the boundary conditions, such as fluctuations in solar input, volcanic activity, land cover and ice shelves, could be expected to produce an excessively-stable simulation.

The second possibility is that natural, decadal- to centennial-timescale changes in air-sea exchange have little impact on atmospheric $\Delta^{14}\text{C}$. This possibility would imply that the production rate of ^{14}C by cosmic rays within the upper atmosphere was the primary driver of observed atmospheric $\Delta^{14}\text{C}$ variability during the pre-industrial interval

of the Holocene. The latter explanation would be consistent with the arguments put forth by previous workers, including Stuiver and Quay (1980) and Siegenthaler (1980), supported by records of ^{10}Be (Bard et al., 2000; Muscheler et al., 2007) and commonly assumed by those interpreting the atmospheric radiocarbon record as an indicator of solar output over the Holocene (Knudsen et al., 2009). This reassuring consistency simultaneously supports the magnitude of variability exhibited by the model, while helping to simplify the interpretation of both atmospheric and oceanic records of $\Delta^{14}\text{C}$.

6. Conclusions

The CM2Mc model simulation explored here exhibits modes of interannual variability similar to ENSO and the SAM, as characterized by observations. Overall, CM2Mc's tropical and ENSO biases are qualitatively similar in character to those seen in the higher-resolution model, CM2.1 (Wittenberg, 2009), though somewhat larger in amplitude. This suggests CM2Mc may provide a cost-effective new tool to explore the causes of these biases, which are shared among many state-of-the-art CGCMs (Guilyardi et al., 2009), and which complicate future projections of tropical climate and ENSO (Collins et al., 2010; Vecchi and Wittenberg, 2010).

The distribution of radiocarbon within the model was well correlated with these modes of interannual variability, with distinct relationships linking tropical ^{14}C to NINO3 SST. The modeled surface water $\Delta^{14}\text{C}$ at the Galapagos site (Figure 14) is remarkably stable in comparison to the observed variability (Figure 1), suggesting that the unforced model underestimates true variability, perhaps due to difficulties in capturing the local details of the equatorial current structure of Galapagos, a possibility that we leave to

further investigation. In contrast, the vicinity of the ITF stands out as a particularly sensitive location in which to use coral $\Delta^{14}\text{C}$ as a monitor of circulation changes (Figure 14), due to the coincidence of strong $\Delta^{14}\text{C}$ gradients with variable water transport.

Meanwhile, the variability of ^{14}C in the Southern Ocean was dominated by changes in deep convection on a multi-decadal timescale. In the model, these convection events are independent of the relatively high-frequency SAM, but are associated with dramatic changes in sea surface salinity. In the Weddell Sea, salty anomalies originate near the prime meridian due to atmospheric forcing, and advect southwestwards towards the gyre center where they set off vigorous convection. The convection brings warm, ^{14}C -depleted deep water to the surface, until the halocline re-establishes itself (Figure 14). Given the difficulty of representing convection accurately in a global, level-coordinate ocean model with unrealistically-stable boundary conditions, the details of this mechanism must be regarded with some caution. Indeed, they are reminiscent of ‘flushing’ events, noted in coarse resolution models with mixed boundary conditions (Winton and Sarachik, 1993), and may reflect the inability of the model to produce dense waters on shelves, as would occur in nature (Toggweiler et al., 2006). Nonetheless, their common occurrence in global climate models warrants attention, and can be effectively diagnosed using radiocarbon.

Although the simulated changes in $\Delta^{14}\text{C}$ in the Southern Ocean were relatively dramatic, the resulting air-sea fluxes of ^{14}C and ^{12}C , quantified as a disequilibrium flux, were insufficient to alter atmospheric $\Delta^{14}\text{C}$ by more than a few permil (Figure 14), far less than the magnitude of the Suess wiggles (O 20 ‰, Figure 1). One might suggest that this discrepancy indicates that natural variability in the climate system, produced by

external forcings or internal feedbacks, significantly exceeds that of the model. However, previous authors have presented substantial evidence that the Suess wiggles were dominated by changes in the production rate of ^{14}C , caused by fluctuations in the geomagnetic field and solar activity (Stuiver and Quay, 1980; Bard et al., 2000; Muscheler et al., 2007), and the results here are fully consistent with this.

We note that at the end of the last ice age, long before the recent Suess wiggles, atmospheric $\Delta^{14}\text{C}$ declined by a large amount, most notably by 190 ‰ during the ‘Mystery Interval’ between ~17.5 and 14.5 ky ago (Broecker and Barker, 2007). It has been frequently suggested that vertical mixing in the Southern Ocean allowed abyssal ^{14}C -depleted water to leak into the atmosphere at this time (Hughen et al, 1998; Marchitto et al., 2007). For comparison, the convective events displayed by the model here would drive a change in atmospheric $\Delta^{14}\text{C}$ of only ~10 ‰, if sustained over millennia and allowed to equilibrate with other C reservoirs. The Mystery Interval therefore requires that a very ^{14}C -depleted reservoir have been tapped at this time, which appears to have included a poorly-ventilated glacial abyssal ocean (Galbraith et al., 2007; Skinner et al., 2010) but may have involved additional reservoirs as well.

In closing, we emphasize the utility of radiocarbon as an Earth system tracer. Its inclusion in the simulations shown here provides diagnostic information on the model performance, particularly regarding the ventilation of the deep ocean, as well as the ability to compare directly with coral records of tropical climate variability. Further modeling work could explore the way in which changes in the atmospheric production rate of ^{14}C propagate through the ocean, while we highlight the potential for further high-

resolution coral records from the Indonesian Throughflow region to help characterize natural climate variability in the pre-instrumental period.

Acknowledgments.

We thank Ellen Druffel for providing coral data and for comments on an early draft of the manuscript, and Michael Winton, Matthew Harrison, and Hyo-Seok Park for discussions. Robbie Toggweiler and Stephanie Downes provided internal reviews. The OAA_OI_SST_V2 data was provided by the NOAA/OAR/ESRL PSD, Boulder, Colorado, USA, from their Web site at <http://www.esrl.noaa.gov/psd/> and ECMWF ERA-40 data were provided by ECMWF/have been obtained from the ECMWF Data Server. This work was funded by NOAA, NSF and NSERC.

References

- Adcroft, A., C. Hill, and J. Marshall, 1997: Representation of topography by shaved cells in a height coordinate ocean model. *Monthly Weather Review*, **125**, 2293-2315.
- Adcroft, A., J. M. Campin, C. Hill, and J. Marshall, 2004: Implementation of an atmosphere-ocean general circulation model on the expanded spherical cube. *Monthly Weather Review*, **132**, 2845-2863.
- Anderson, J. L., and Coauthors, 2004: The new GFDL global atmosphere and land model AM2-LM2: Evaluation with prescribed SST simulations. *Journal of Climate*, **17**, 4641-4673.
- Antonov, J. I., R. A. Locarnini, T. P. Boyer, A. V. Mishonov, and H. E. Garcia, 2006: *World Ocean Atlas 2005, Volume 2: Salinity*. U.S. Government Printing Office, 182 pp.
- Bacastow, R., and E. Maier-Raimer, 1990: Ocean-circulation model of the carbon cycle. *Climate Dynamics*, **4**, 95-125.
- Bard, E., G. Raisbeck, F. Yiou, and J. Jouzel, 2000: Solar irradiance during the last 1200 years based on cosmogenic nuclides. *Tellus*, **52B**, 985-992.
- Boning, C. W., A. Dispert, M. Visbeck, S. R. Rintoul, and F. U. Schwarzkopf, 2008: The response of the Antarctic Circumpolar Current to recent climate change. *Nature Geoscience*, **1**, 864-869.
- Bretherton, C. S., M. Widmann, V. P. Dymnikov, J. M. Wallace, and I. Blade, 1999: The effective number of spatial degrees of freedom of a time-varying field. *Journal of Climate*, **12**, 1990-2009.

- 645 Broecker, W., and S. Barker, 2007: A 190 permil drop in atmosphere's Delta 14-C during
 646 the "Mystery Interval" (17.5 to 14.5 kyr). *Earth and Planetary Science Letters*, **256**, 90-
 647 99.
- 648 Collins, M., and Coauthors, 2010: The impact of global warming on the tropical Pacific
 649 and El Niño. *Nature Geoscience*, **3**, 391-397.
- 650 Conkright, M. E., R. A. Locarnini, H. E. Garcia, T. D. O'Brien, T. P. Boyer, C. Stephens,
 651 and J. I. Antonov, 2002: World Ocean Atlas 2001: Objective Analysis, Data Statistics and
 652 Figures, CD-ROM. *National Oceanographic Data Center, Silver Spring*.
- 653 Cunningham, S. A., S. G. Alderson, B. A. King, and M. A. Brandon, 2003: Transport and
 654 variability of the Antarctic Circumpolar Current in Drake Passage. *Journal of*
 655 *Geophysical Research-Oceans*, **108**.
- 656 De Szoeko, S. P., and S. P. Xie, 2008: The tropical eastern Pacific seasonal cycle:
 657 Assessment of errors and mechanisms in IPCC AR4 coupled ocean - Atmosphere general
 658 circulation models. *Journal of Climate*, **21**, 2573-2590.
- 659 Delworth, T. L., and Coauthors, 2006: GFDL's CM2 global coupled climate models. Part
 660 I: Formulation and simulation characteristics. *Journal of Climate*, **19**, 643-674.
- 661 Domack, E., A. Leventer, R. Dunbar, F. Taylor, S. Brachfeld, C. Sjunneskog, and O. D.
 662 P. L. S. Party, 2001: Chronology of the Palmer Deep site, Antarctic Peninsula: a
 663 Holocene palaeoenvironmental reference for the circum-Antarctic. *Holocene*, **11**, 1-9.
- 664 Dong, S., J. Sprintall, S. T. Gille, and L. Talley, 2008: Southern Ocean mixed-layer depth
 665 from Argo float profiles. *Journal of Geophysical Research*, **113**.
- 666 Druffel, E. R. M., 1997: Geochemistry of corals: Proxies of past ocean chemistry, ocean
 667 circulation, and climate. *Proc. Natl. Acad. Sci. U. S. A.*, **94**, 8354-8361.

- 668 Druffel, E. R. M., S. Griffin, S. R. Beaupre, and R. B. Dunbar, 2007: Oceanic climate and
 669 circulation changes during the past four centuries from radiocarbon in corals.
 670 *Geophysical Research Letters*, **34**.
- 671 Druffel, E. R. M., and Coauthors, 2004: Variability of monthly radiocarbon during the
 672 1760s in corals from the Galapagos Islands. *Radiocarbon*, **46**, 627-631.
- 673 Duffy, P. B., K. Caldeira, J. Selvaggi, and M. I. Hoffert, 1997: Effects of subgrid-scale
 674 mixing parameterizations on simulated distributions of natural C-14, temperature, and
 675 salinity in a three-dimensional ocean general circulation model. *Journal of Physical*
 676 *Oceanography*, **27**, 498-523.
- 677 Fallon, S. J., and T. P. Guilderson, 2008: Surface water processes in the Indonesian
 678 throughflow as documented by a high-resolution coral Delta C-14 record. *Journal of*
 679 *Geophysical Research-Oceans*, **113**.
- 680 Farnetti, R., T. L. Delworth, A. Rosati, S. Griffies, and F. Zeng, 2010: The role of
 681 mesoscale eddies in the rectification of the Southern Ocean response to climate change.
 682 *Journal of Physical Oceanography*, **in press**.
- 683 Fukamachi, Y., S. Rintoul, J. A. Church, K. Aoki, A. Sokolov, M. A. Rosenberg, and M.
 684 Wakatsuchi, 2010: Strong export of Antarctic Bottom Water east of the Kerguelen
 685 plateau. *Nature Geoscience*, **3**, 327-331.
- 686 Galbraith, E. D., A. Gnanadesikan, J. Dunne, and M. R. Hiscock, 2010: Regional impacts
 687 of iron-light colimitation in a global biogeochemical model. *Biogeosciences*, **7**, 1043-
 688 1064.
- 689 Galbraith, E. D., and Coauthors, 2007: Carbon dioxide release from the North Pacific
 690 abyss during the last deglaciation. *Nature*, **449**, 890-U899.

- 691 Gent, P. R., and J. C. McWilliams, 1990: Isopycnal mixing in ocean circulation models.
 692 *Journal of Physical Oceanography*, **20**, 150-155.
- 693 Ginoux, P., L. W. Horowitz, V. Ramaswamy, I. V. Geogdzhayev, B. N. Holben, G.
 694 Stenchikov, and X. Tie, 2006: Evaluation of aerosol distribution and optical depth in the
 695 Geophysical Fluid Dynamics Laboratory coupled model CM2.1 for present climate.
 696 *Journal of Geophysical Research-Atmospheres*, **111**.
- 697 Gnanadesikan, A., S. M. Griffies, and B. L. Samuels, 2007: Effects in a climate model of
 698 slope tapering in neutral physics schemes. *Ocean Modelling*, **16**, 1-16.
- 699 Gnanadesikan, A., J. P. Dunne, R. M. Key, K. Matsumoto, J. L. Sarmiento, R. D. Slater,
 700 and P. S. Swathi, 2004: Oceanic ventilation and biogeochemical cycling: Understanding
 701 the physical mechanisms that produce realistic distributions of tracers and productivity.
 702 *Global Biogeochemical Cycles*, **18**.
- 703 Gnanadesikan, A., and Coauthors, 2006: GFDL's CM2 global coupled climate models.
 704 Part II: The baseline ocean simulation. *Journal of Climate*, **19**, 675-697.
- 705 Griffies, S., and Coauthors, 2005: Formulation of an ocean model for global climate
 706 simulations. *Ocean Science*, **1**, 45-79.
- 707 Griffies, S. M., 2009: Elements of MOM4p1. *GFDL Ocean Group Technical Report*, **6**,
 708 444.
- 709 Grumet, N. S., P. B. Duffy, M. E. Wickett, K. Caldeira, and R. B. Dunbar, 2005:
 710 Intrabasin comparison of surface radiocarbon levels in the Indian Ocean between coral
 711 records and three-dimensional global ocean models. *Global Biogeochemical Cycles*, **19**.
- 712 Guilderson, T. P., K. Caldeira, and P. B. Duffy, 2000: Radiocarbon as a diagnostic tracer
 713 in ocean and carbon cycle modeling. *Global Biogeochemical Cycles*, **14**, 887-902.

- 714 Guilderson, T. P., D. P. Schrag, M. Kashgarian, and J. Southon, 1998: Radiocarbon
 715 variability in the western equatorial Pacific inferred from a high-resolution coral record
 716 from Nauru Island. *Journal of Geophysical Research-Oceans*, **103**, 24641-24650.
- 717 Guilderson, T. P., S. Fallon, M. D. Moore, D. P. Schrag, and C. D. Charles, 2009:
 718 Seasonally resolved surface water $\Delta^{14}\text{C}$ variability in the Lombok Strait: A coralline
 719 perspective. *Journal of Geophysical Research-Oceans*, **114**.
- 720 Guilyardi, E., and Coauthors, 2009: Understanding El Niño in ocean-atmosphere general
 721 circulation models: Progress and Challenges. *Bulletin of the American Meteorological*
 722 *Society*, **90**, 325-+.
- 723 Hall, A., and M. Visbeck, 2002: Synchronous variability in the southern hemisphere
 724 atmosphere, sea ice, and ocean resulting from the annular mode. *Journal of Climate*, **15**,
 725 3043-3057.
- 726 Haywood, J. M., V. Ramaswamy, and B. J. Soden, 1999: Tropospheric aerosol climate
 727 forcing in clear-sky satellite observations over the oceans. *Science*, **283**, 1299-1303.
- 728 Huguen, K. A., and Coauthors, 1998: Deglacial changes in ocean circulation from an
 729 extended radiocarbon calibration. *Nature*, **391**, 65-68.
- 730 Key, R. M., and Coauthors, 2004: A global ocean carbon climatology: Results from
 731 Global Data Analysis Project (GLODAP). *Global Biogeochemical Cycles*, **18**,
 732 doi:10.1029/2004GB002247.
- 733 Knudsen, M. F., P. Riisager, B. H. Jacobsen, R. Muscheler, I. Snowball, and M. S.
 734 Seidenkrantz, 2009: Taking the pulse of the Sun during the Holocene by joint analysis of
 735 C-14 and Be-10. *Geophysical Research Letters*, **36**.

- 736 Large, W. G., J. C. McWilliams, and S. C. Doney, 1994: Oceanic vertical mixing - a
 737 review and a model with a nonlocal boundary-layer parameterization. *Reviews of*
 738 *Geophysics*, **32**, 363-403.
- 739 Lee, H. C., A. Rosati, and M. J. Spelman, 2006: Barotropic tidal mixing effects in a
 740 coupled climate model: Oceanic conditions in the Northern Atlantic. *Ocean Modelling*,
 741 **11**, 464-477.
- 742 Leventer, A., E. W. Domack, S. E. Ishman, S. Brachfeld, C. E. McClennen, and P.
 743 Manley, 1996: Productivity cycles of 200-300 years in the Antarctic Peninsula region:
 744 Understanding linkages among the sun, atmosphere, oceans, sea ice, and biota.
 745 *Geological Society of America Bulletin*, **108**, 1626-1644.
- 746 Lin, S.-J., 2004: A "vertically Lagrangian" finite-volume dynamical core for global
 747 models. *Monthly Weather Review*, **132**, 2293-2307.
- 748 Locarnini, R. A., A. V. Mishonov, J. I. Antonov, T. P. Boyer, and H. E. Garcia, 2006:
 749 *World Ocean Atlas 2005, Volume 1: Temperature*. U.S. Government Printing Office, 182
 750 pp.
- 751 Manizza, M., C. Le Quere, A. J. Watson, and E. T. Buitenhuis, 2005: Bio-optical
 752 feedbacks among phytoplankton, upper ocean physics and sea-ice in a global model.
 753 *Geophysical Research Letters*, **32**.
- 754 Marchitto, T., S. J. Lehman, J. D. Ortiz, J. Fluckiger, and A. van Geen, 2007: Marine
 755 radiocarbon evidence for the mechanism of deglacial atmospheric CO₂ rise. *Science*, **316**,
 756 1456-1459.
- 757 Marshall, G. J., 2002: Analysis of recent circulation and thermal advection change in the
 758 northern Antarctic Peninsula. *International Journal of Climatology*, **22**, 1557-1567.

- 759 Masarik, J., and J. Beer, 1999: Simulation of particle fluxes and cosmogenic nuclide
760 production in the Earth's atmosphere. *Journal of Geophysical Research-Atmospheres*,
761 **104**, 12099-12111.
- 762 Matsumoto, K., and Coauthors, 2004: Evaluation of ocean carbon cycle models with
763 data-based metrics. *Geophysical Research Letters*, **31**.
- 764 Milly, P. C. D., and A. B. Shmakin, 2002: Global modeling of land water and energy
765 balances. Part I: the land dynamics (LaD) model. *Journal of Hydrometeorology*, **3**, 283-
766 299.
- 767 Murray, R. J., 1996: Explicit generation of orthogonal grids for ocean models. *J Comput*
768 *Phys*, **126**, 251-273.
- 769 Muscheler, R., F. Joos, J. Beer, S. A. Muller, M. Vonmoos, and I. Snowball, 2007: Solar
770 activity during the last 1000 yr inferred from radionuclide records. *Quaternary Science*
771 *Reviews*, **26**, 82-97.
- 772 Najjar, R., and J. C. Orr, 1998: Design of OCMIP-2 simulations of chlorofluorocarbons,
773 the solubility pump and common biogeochemistry.
- 774 Naveira Garabato, A. C., K. L. Polzin, B. A. King, K. J. Heywood, and M. Visbeck,
775 2004: Widespread intense turbulent mixing in the Southern Ocean. *Science*, **303**, 210-
776 213.
- 777 Pacanowski, R. C., and A. Gnanadesikan, 1998: Transient response in a z-level ocean
778 model that resolves topography with partial cells. *Monthly Weather Review*, **126**, 3248-
779 3270.
- 780 Redfield, A. C., B. H. Ketchum, and F. A. Richards, 1963: The influence of organisms on
781 the composition of sea-water. *The Sea*, M. N. Hill, Ed., John Wiley & Sons, 26-77.

- 782 Reimer, P. J., and Coauthors, 2004: IntCal04 terrestrial radiocarbon age calibration, 0-26
783 cal kyr BP. *Radiocarbon*, **46**, 1029-1058.
- 784 Reynolds, R. W., N. A. Rayner, T. M. Smith, D. C. Stokes, and W. Wang, 2002: An
785 improved in situ and satellite SST analysis for climate. *Journal of Climate*, **15**, 1609-
786 1625.
- 787 Rodgers, K. B., M. A. Cane, and D. P. Schrag, 1997: Seasonal variability of sea surface
788 Delta C-14 in the equatorial Pacific in an ocean circulation model. *Journal of*
789 *Geophysical Research-Oceans*, **102**, 18627-18639.
- 790 Rodgers, K. B., D. P. Schrag, M. A. Cane, and N. H. Naik, 2000: The bomb C-14
791 transient in the Pacific Ocean. *Journal of Geophysical Research-Oceans*, **105**, 8489-
792 8512.
- 793 Rodgers, K. B., and Coauthors, 2004: Radiocarbon as a thermocline proxy for the eastern
794 equatorial Pacific. *Geophysical Research Letters*, **31**.
- 795 Rubin, S. I., and R. M. Key, 2002: Separating natural and bomb-produced radiocarbon in
796 the ocean: The potential alkalinity method. *Global Biogeochemical Cycles*, **16**.
- 797 Shackleton, N. J., J. C. Duplessy, M. Arnold, P. Maurice, M. A. Hall, and J. Cartlidge,
798 1988: Radiocarbon age of last glacial Pacific deep water. *Nature*, **335**, 708-711.
- 799 Siegenthaler, U., M. Heimann, and H. Oeschger, 1980: C-14 variations caused by
800 changes in the global carbon cycle. *Radiocarbon*, **22**, 177-191.
- 801 Simmons, H. L., S. R. Jayne, L. C. St Laurent, and A. J. Weaver, 2004: Tidally driven
802 mixing in a numerical model of the ocean general circulation. *Ocean Modelling*, **6**, 245-
803 263.

- 804 Skinner, L. C., S. Fallon, C. Waelbroeck, E. Michel, and S. Barker, 2010: Ventilation of
 805 the Deep Southern Ocean and Deglacial CO₂ rise. *Science*, **328**, 1147-1151.
- 806 Smethie, W. M., D. A. LeBel, R. A. Fine, M. Rhein, and D. Kieke, 2007: On Past and
 807 future changes of the Ocean's Meridional Overturning Circulation. *Past and Future*
 808 *Changes of the Ocean's Meridional Overturning Circulation: Mechanisms and Impacts*, A.
 809 Schmittner, J. Chiang, and S. Hemming, Eds., AGU Geophysical Monograph Series, 119-
 810 130.
- 811 Stuiver, M., and H. A. Polach, 1977: Reporting of ¹⁴C data. *Radiocarbon*, **19**, 355-363.
- 812 Stuiver, M., and P. D. Quay, 1980: Changes in atmospheric C-14 attributed to a variable
 813 sun. *Science*, **207**, 11-19.
- 814 Suess, E., 1953: Natural radiocarbon and the rate of exchange of carbon dioxide between
 815 the atmosphere and the sea. *Nuclear processes in geologic settings*, N. R. C. C. o. N.
 816 Science, Ed., University of Chicago Press, 52-56.
- 817 —, 1968: Climatic changes, solar activity, and the cosmic-ray production rate of the
 818 natural radiocarbon. *Meteorology Monthly*, **8**, 146-150.
- 819 Tillinger, D., and A. L. Gordon, 2009: Fifty Years of the Indonesian Throughflow.
 820 *Journal of Climate*, **22**, 6342-6355.
- 821 Toggweiler, J. R., and B. Samuels, 1993: New Radiocarbon Constraints on the Upwelling
 822 of Abyssal Water to the Ocean's Surface. *The Global Carbon Cycle*, M. Heimann, Ed.,
 823 Springer-Verlag, 333-365.
- 824 Toggweiler, J. R., K. Dixon, and K. Bryan, 1989: Simulations of radiocarbon in a coarse-
 825 resolution world ocean model 1: Steady-state prebomb distributions. *Journal of*
 826 *Geophysical Research-Oceans*, **94**, 8217-8242.

- 827 Toggweiler, J. R., K. Dixon, and W. S. Broecker, 1991: The Peru Upwelling and the
828 Ventilation of the South-Pacific Thermocline. *Journal of Geophysical Research-Oceans*,
829 **96**, 20467-20497.
- 830 Toggweiler, J. R., J. L. Russell, and S. R. Carson, 2006: Midlatitude westerlies,
831 atmospheric CO₂, and climate change during the ice ages. *Paleoceanography*, **21**.
- 832 Vecchi, G. A., and A. T. Wittenberg, 2010: El Niño and our future climate: Where do we
833 stand? *Wiley Interdisciplinary Reviews: Climate Change*, **1**, 260-270.
- 834 Visbeck, M., 2009: A Station-Based Southern Annular Mode Index from 1884 to 2005.
835 *Journal of Climate*, **22**, 940-950.
- 836 Wanninkhof, R., 1992: Relationship between wind-speed and gas-exchange over the
837 ocean. *Journal of Geophysical Research-Oceans*, **97**, 7373-7382.
- 838 Winton, M., and E. S. Sarachik, 1993: Thermohaline oscillations induced by strong
839 steady salinity forcing of ocean general circulation models. *Journal of Physical*
840 *Oceanography*, **23**, 1389-1410.
- 841 Wittenberg, A. T., 2009: Are historical records sufficient to constrain ENSO simulations?
842 *Geophysical Research Letters*, **36**.
- 843 Wittenberg, A. T., A. Rosati, N. C. Lau, and J. J. Ploshay, 2006: GFDL's CM2 global
844 coupled climate models. Part III: Tropical pacific climate and ENSO. *Journal of Climate*,
845 **19**, 698-722.

846 **List of Figures**

847 FIG. 1. Observational reconstructions of $\Delta^{14}\text{C}$ in the atmosphere and ocean. The top
 848 shows atmospheric $\Delta^{14}\text{C}$ for the northern hemisphere (orange, (Reimer et al., 2004)) and
 849 the southern hemisphere (red) over 1500-1900 AD, reconstructed from tree ring archives.
 850 The bottom shows reconstructed $\Delta^{14}\text{C}$ of surface water at Galapagos, reconstructed from
 851 fossil coral (Druffel et al., 2007). Measurement errors are shown as reported.

852 FIG. 2: Atmospheric simulation of CM2Mc. Annual precipitation (left column, mm d^{-1})
 853 and net radiative balance across the top of the atmosphere (W m^{-2}), from
 854 CM2Mc and observation-based estimates. Top row shows model simulation, center row
 855 shows observations of precipitation (CMAPv2+rain gauge estimates) and radiative
 856 balance (ERBE), bottom row shows the difference between model and observations.

857 FIG. 3: Annual mean temperature and salinity errors of CM2Mc. Top row, sea surface
 858 temperature and salinity errors, compared to observations (Antonov et al., 2006;
 859 Locarnini et al., 2006). Bottom row, average temperature and salinity errors over the
 860 upper 1500 m of the water column.

861 FIG. 4: Meridional overturning circulation of CM2Mc. Top left, global overturning
 862 streamfunction as a function of depth. Top right, global overturning streamfunction as a
 863 function of density. Bottom left, overturning streamfunction for the IndoPacific. Bottom
 864 right, overturning streamfunction for the Atlantic. All panels plotted in Sv.

865 FIG. 5: Phosphate simulation of iBGC in CM2Mc. The left column shows observed
 866 phosphate concentrations (Conkright et al., 2002), while the right column shows model
 867 output. The middle row shows a zonal average between 30W and 0, in the Atlantic

868 Ocean, while the lower row shows a zonal average between 180W and 150W, in the
 869 Pacific Ocean.

870 FIG. 6: Radiocarbon simulation in the ocean of CM2Mc. The left column shows the
 871 GLODAP background $\Delta^{14}\text{C}$ activities, for which the pre-bomb activity is estimated by a
 872 calibrated alkalinity regression (Key et al., 2004). The right column shows the
 873 corresponding model output. The top row shows the ocean surface; the greater regional
 874 variability in the model may reveal small-scale circulation features lost in the heavily
 875 smoothed observation-based regression, while the generally higher values in the model
 876 are expected from the effect of fossil fuel invasion (see text). Zonal averages correspond
 877 to those of Figure 5.

878 FIG. 7: Unforced variability in the simulation of temperature and $\Delta^{14}\text{C}$ at the sea surface.
 879 Top left, standard deviation of monthly-averaged $\Delta^{14}\text{C}$. Top right, correlation between
 880 surface $\Delta^{14}\text{C}$ and the globally averaged SST. Lower row, correlations between $\Delta^{14}\text{C}$ and
 881 both high-and low-pass filtered global SST (cutoff frequency 20y). All panels use
 882 monthly-averaged values of SST and/or $\Delta^{14}\text{C}$ over a continuous 500-year time interval.
 883 Note that large deviations of $\Delta^{14}\text{C}$, correlated with global temperatures, are found in both
 884 the vicinity of Indonesia and the high latitude Southern Ocean.

885 FIG. 8: Simulation of unforced ENSO-like variability. Top left, frequency spectrum of
 886 SST in the NINO3 region, observations (ERA40 reanalysis, black) and CM2Mc (red,
 887 dashed). Top right, regression of SST on NINO3 SST, observations (ERA40 reanalysis,
 888 colours) and CM2Mc (contours). Bottom left, as in top right, showing zonal wind stress
 889 on the ocean (N m^{-2}). Bottom right, as in top right, showing wind stress curl.

FIG. 9: Phasing between NINO3 SST and temperature or $\Delta^{14}\text{C}$ at the sea surface. The top row shows 6-month lead correlations between the indicated variable and NINO3 SST, the center row shows in phase correlations, and the bottom row shows 6-month lag correlations. The left column shows the regressions of observed SST (Reynolds et al., 2002), the center column shows the corresponding regressions for model SST, and the right column shows the regressions for model $\Delta^{14}\text{C}$.

FIG. 10: Model simulation of SAM-like variability. The first Empirical Orthogonal Function (EOF) of the monthly sea level pressure anomaly south of 20°S is shown, as obtained from observations (ERA40, left) and model (right).

FIG. 11: Regression of simulated sea surface $\Delta^{14}\text{C}$ on SAM index. The annual mean SSH contours of -0.4 m (north) and -1.2 m (south) are superimposed in black solid lines to indicate the ACC after Dong et al. (2008). Although there is a negative correlation between surface $\Delta^{14}\text{C}$ and the SAM in the Pacific sector of the Southern Ocean, it explains only a very small amount of the variance, which is due instead to episodic convection.

FIG. 12: Episodic convection events in the Weddell Sea. (a) Water temperature at two depths vs. surface $\Delta^{14}\text{C}$, averaged annually over $50\text{-}30^\circ\text{W}$, $70\text{-}60^\circ\text{S}$. When convection is active, the surface $\Delta^{14}\text{C}$ is low (left side of panel) and the surface is relatively warm, but the water at 300m is relatively cool. (b) As in (a), but showing salt instead of temperature. Panels (c) through (f) show the progression of salinity anomalies (colour) in association with ventilation events, as identified by the rate of change of water age on a 300m depth surface between $50^\circ\text{W}\text{-}30^\circ\text{W}$ and $70^\circ\text{S}\text{-}60^\circ\text{S}$. Dashed contours show surface $\Delta^{14}\text{C}$, in permil.

FIG. 13: Interannual variability in the air-sea radiocarbon fluxes. The interannual variability of surface $\Delta^{14}\text{C}$ (1 s.d.), zonally averaged, is shown by the solid line (right axis). The interannual variability of the disequilibrium flux (1 s.d.), zonally integrated, is shown by the dashed line (left axis).

FIG. 14: Simulated atmospheric and seawater $\Delta^{14}\text{C}$ arising from unforced model variability over 400 years. The upper curve (red) approximates the variations in atmospheric $\Delta^{14}\text{C}$ expected from the simulated air-sea disequilibrium flux, as described in the text. The lower curves show the simulated variations in sea surface $\Delta^{14}\text{C}$ in the model (blue, Galapagos; green, eastern Indian Ocean, near the Lombok Strait; grey, central Weddell Sea). The axes are scaled to be approximately equivalent to the corresponding data shown in Figure 1.

924 TABLE 1. Parameter values used in the iBGC biogeochemical model.

<i>Variable</i>	<i>Description</i>	<i>Value</i>	<i>Units</i>
k	Temperature dependence of growth	0.0378	$^{\circ}\text{C}^{-1}$
k_r	Temperature dependence of remineralization	0.0249	$^{\circ}\text{C}^{-1}$
v_{\max}	Maximum PO_4 uptake rate at 0 $^{\circ}\text{C}$	0.0216	$\mu\text{mol kg}^{-1} \text{d}^{-1}$
k_{PO_4}	PO_4 uptake half-saturation constant	0.1	$\mu\text{mol kg}^{-1}$
irr_k	Light half-saturation constant	20	W m^{-2}
ϕ_{DOP}	Fraction of non-particulate uptake to DOM	0.65	unitless
γ_{DOP}	Decay timescale of DOM	2.56	y^{-1}
C:P	Carbon to Phosphorus ratio in organic matter	106	mol C mol P^{-1}
$wsink_o$	Initial sinking rate	12	m d^{-1}
$wsink_{\text{acc}}$	Acceleration rate of sinking with depth	0.09	d^{-1}
γ_{POP}	Remineralization rate of sinking POM	0.04	d^{-1}

925

926

927

928

929 TABLE 2. Ocean model metrics.

<i>Ocean metric</i>	<i>CM2.1</i>	<i>CM2Mc</i>	<i>Obs</i>	<i>Ref</i>
RMSE Temperature 5 m	1.4	1.8	-	WOA05
RMSE Temperature <1500m	1.3	1.5	-	WOA05
RMSE Salinity 5 m	0.82	0.97	-	WOA05
RMSE Salinity <1500m	0.29	0.34	-	WOA05
ACC (Sv)	125	156	135	Cunningham et al., 2003
NADW at 40N (Sv)	25	22	20 +/- 2	Smethie et al., 2007
ITF (Sv)	13	13.5	12 +/- 3	Gordon et al., 2008
Bering Throughflow (Sv)	0.8	0.9	0.8	Woodgate & Aagard, 2005

930

FIGURE 1

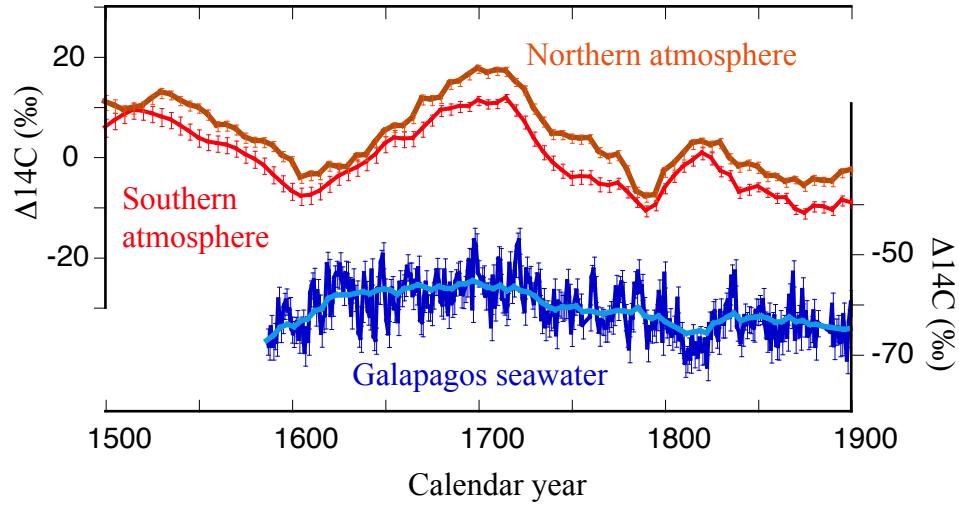


FIG. 1. Observational reconstructions of $\Delta^{14}\text{C}$ in the atmosphere and ocean. The top shows atmospheric $\Delta^{14}\text{C}$ for the northern hemisphere (orange, (Reimer et al., 2004)) and the southern hemisphere (red) over 1500-1900 AD, reconstructed from tree ring archives. The bottom shows reconstructed $\Delta^{14}\text{C}$ of surface water at Galapagos, reconstructed from fossil coral (Druffel et al., 2007). Measurement errors are shown as reported.

FIGURE 2

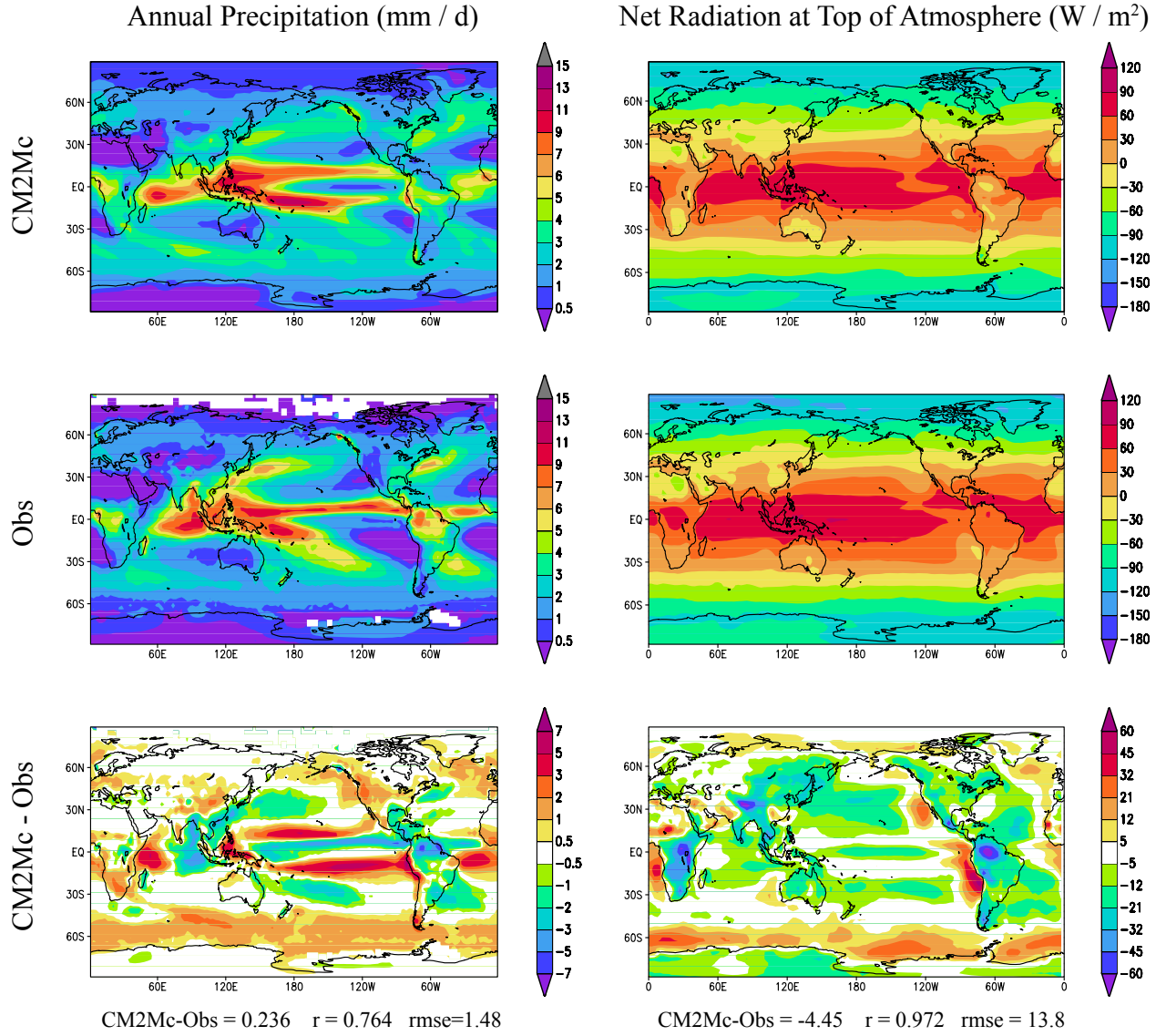


FIG. 2: Atmospheric simulation of CM2Mc. Annual precipitation (left column, mm d-1) and net radiative balance across the top of the atmosphere (right column, W m-2), from CM2Mc and observation-based estimates. Top row shows model simulation, center row shows observations of precipitation (CMAPv2+rain gauge estimates) and radiative balance (ERBE), bottom row shows the difference between model and observations.

FIGURE 3

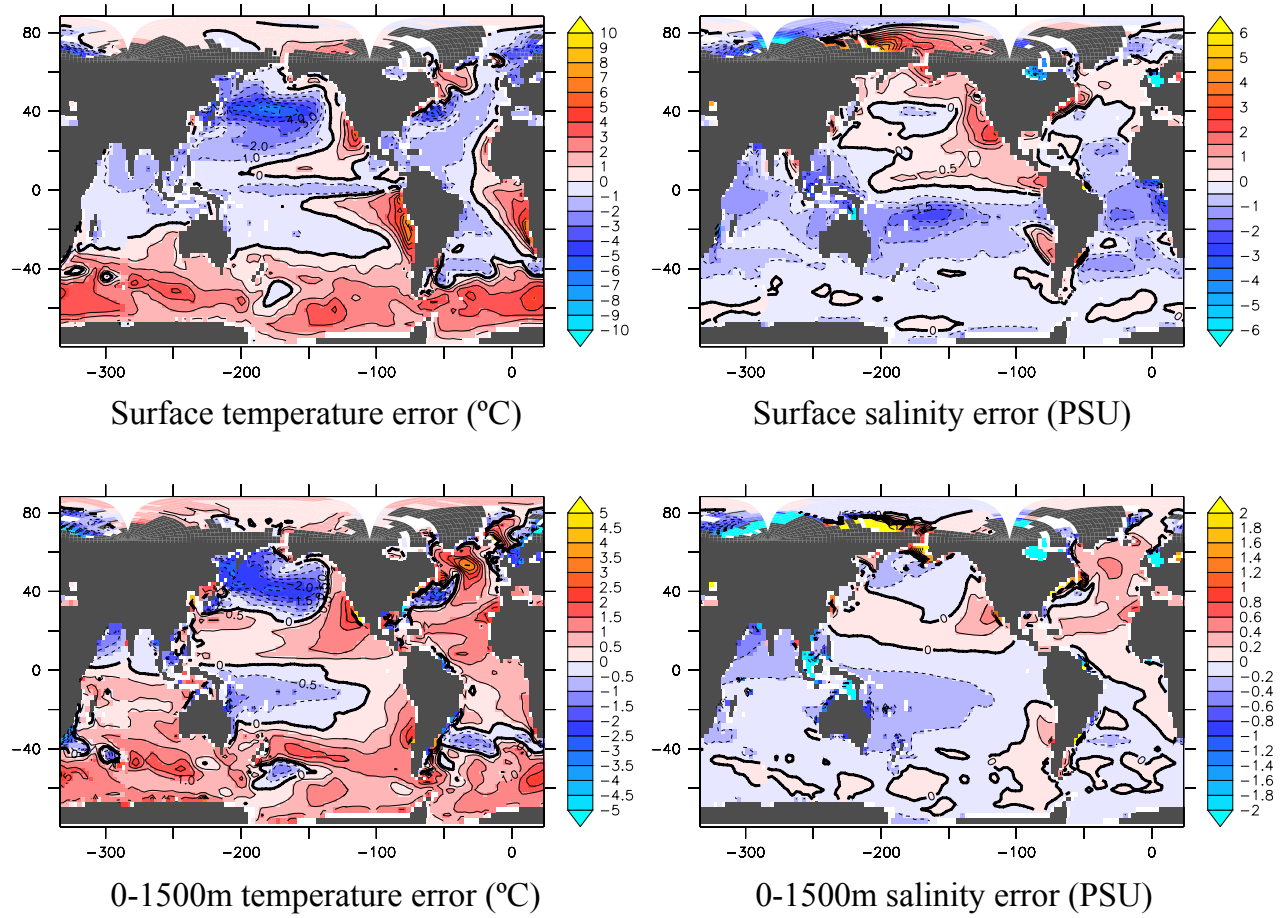


FIG. 3: Annual mean temperature and salinity errors of CM2Mc. Top row, sea surface temperature and salinity errors, compared to observations (Antonov et al., 2006; Locarnini et al., 2006). Bottom row, average temperature and salinity errors over the upper 1500 m of the water column.

FIGURE 4

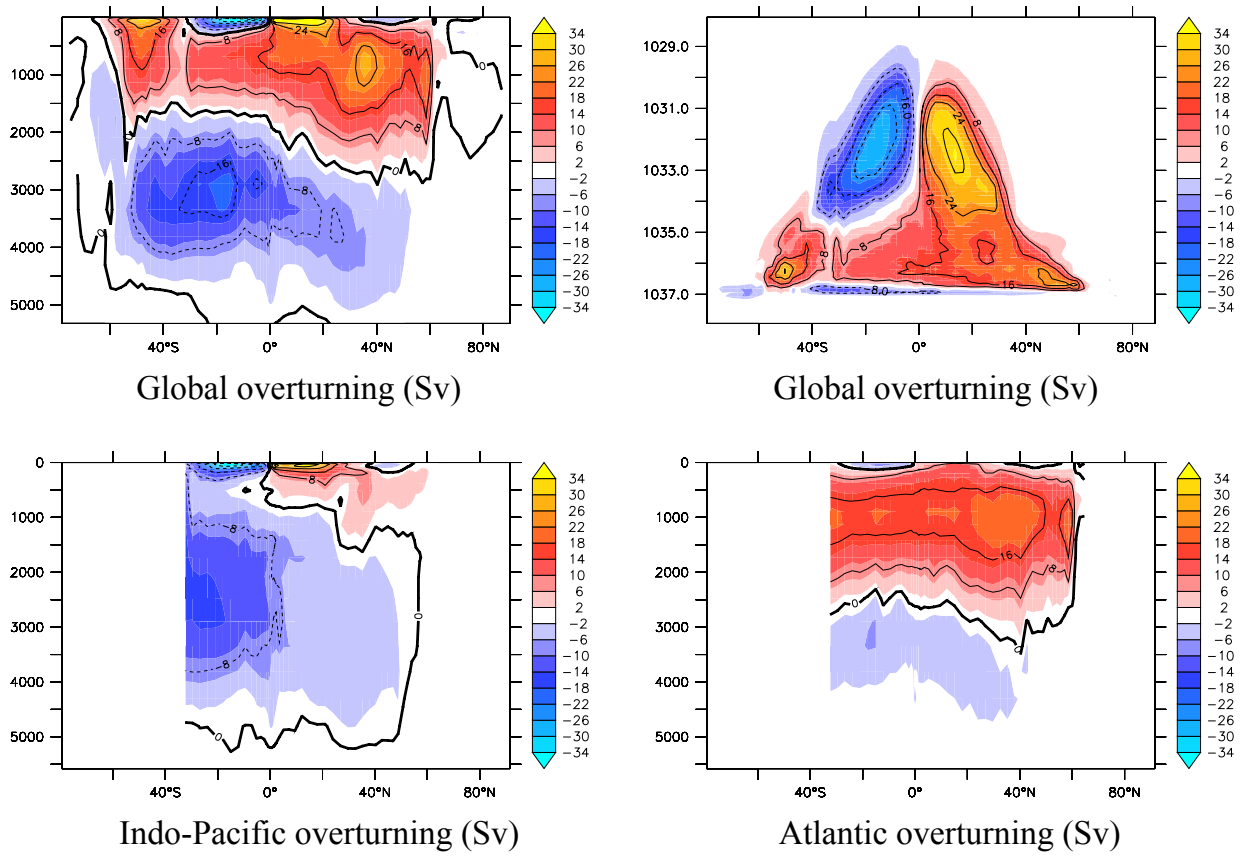


FIG. 4: Meridional overturning circulation of CM2Mc. Top left, global overturning streamfunction as a function of depth. Top right, global overturning streamfunction as a function of density. Bottom left, overturning streamfunction for the IndoPacific. Bottom right, overturning streamfunction for the Atlantic. All panels plotted in Sv.

FIGURE 5

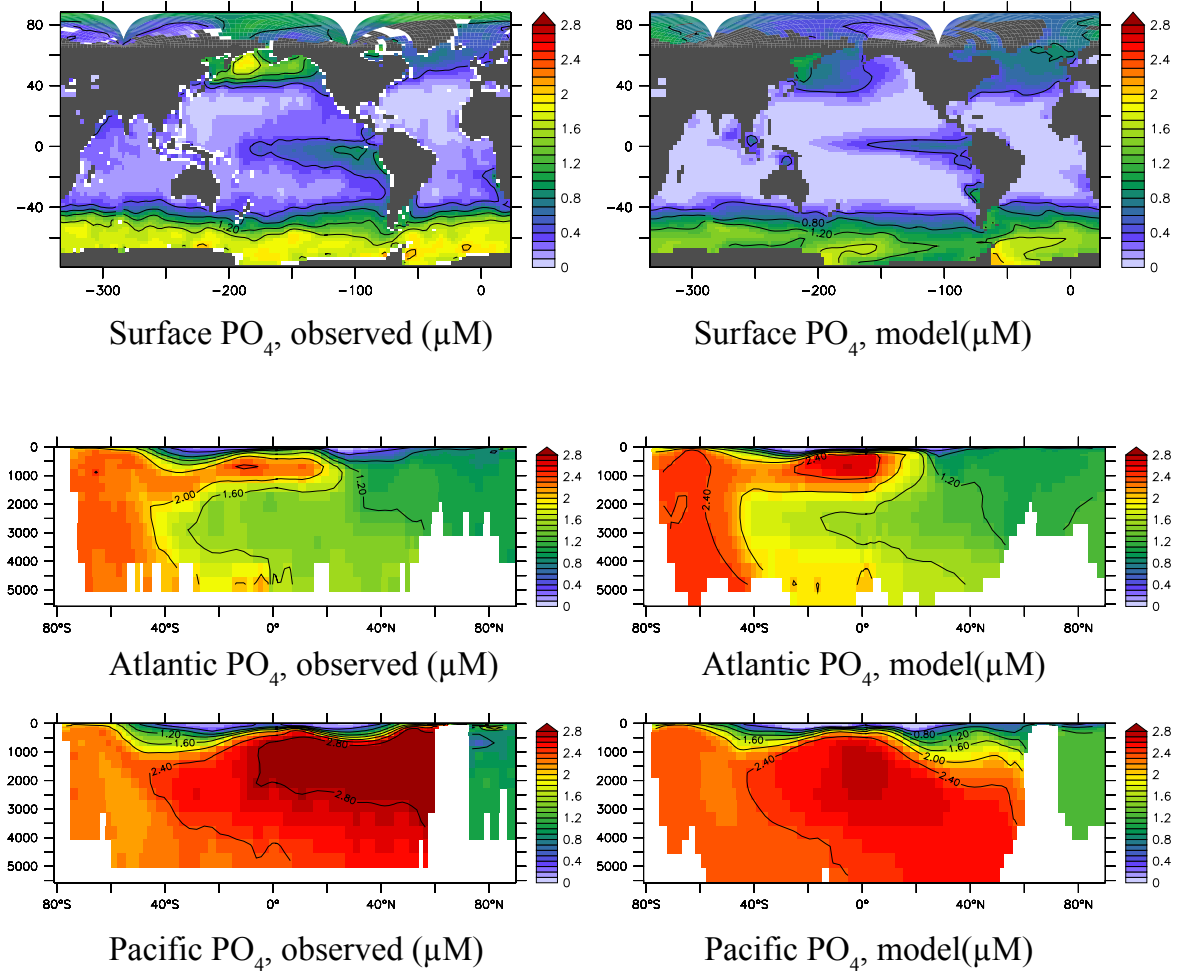


FIG. 5: Phosphate simulation of iBGC in CM2Mc. The left column shows observed phosphate concentrations (Conkright et al., 2002), while the right column shows model output. The middle row shows a zonal average between 30W and 0, in the Atlantic Ocean, while the lower row shows a zonal average between 180W and 150W, in the Pacific Ocean.

FIGURE 6

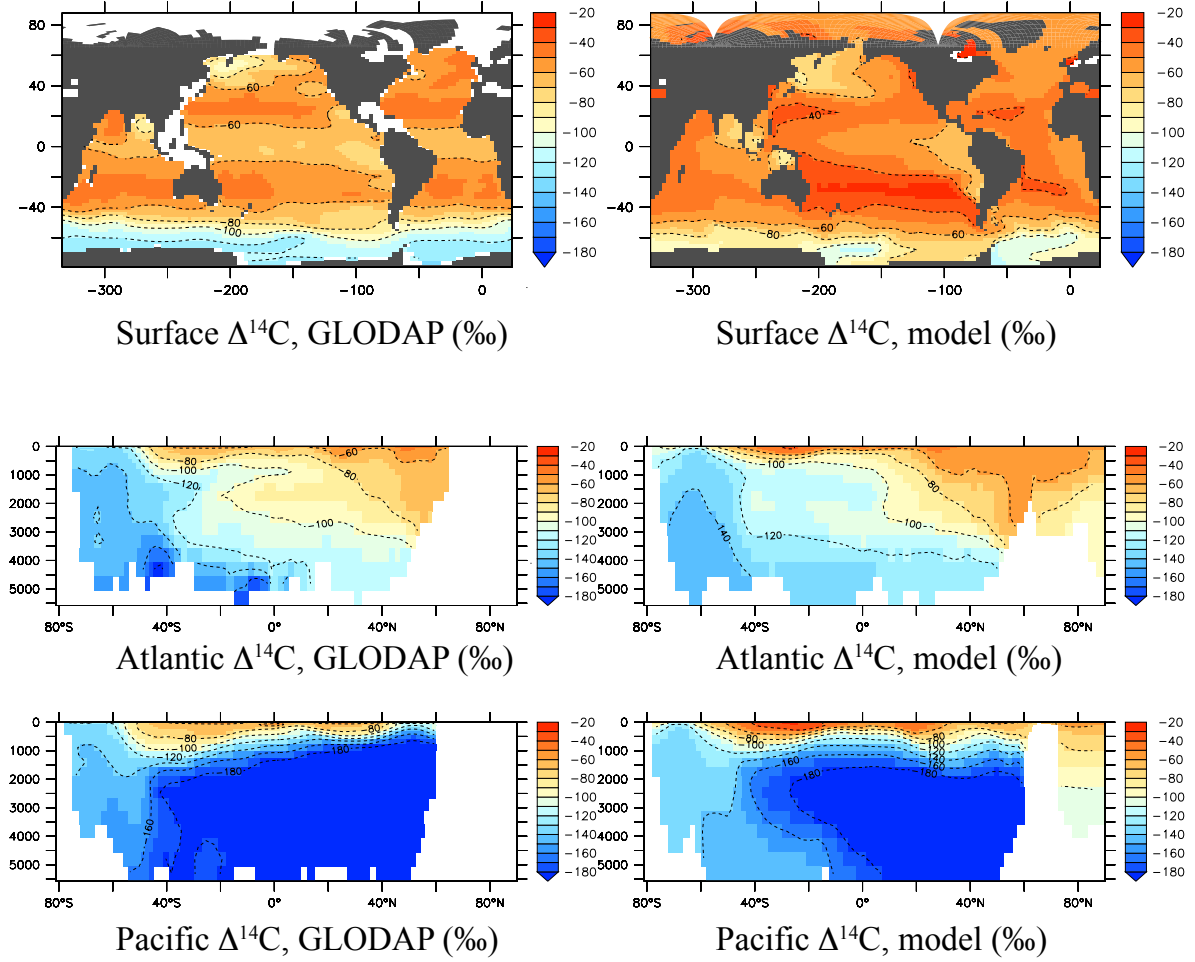


FIG. 6: Radiocarbon simulation in the ocean of CM2Mc. The left column shows the GLODAP background $\Delta^{14}\text{C}$ activities, for which the pre-bomb activity is estimated by a calibrated alkalinity regression (Key et al., 2004). The right column shows the corresponding model output. The top row shows the ocean surface; the greater regional variability in the model may reveal small-scale circulation features lost in the heavily smoothed observation-based regression, while the generally higher values in the model are expected from the effect of fossil fuel invasion (see text). Zonal averages correspond to those of Figure 5.

FIGURE 7

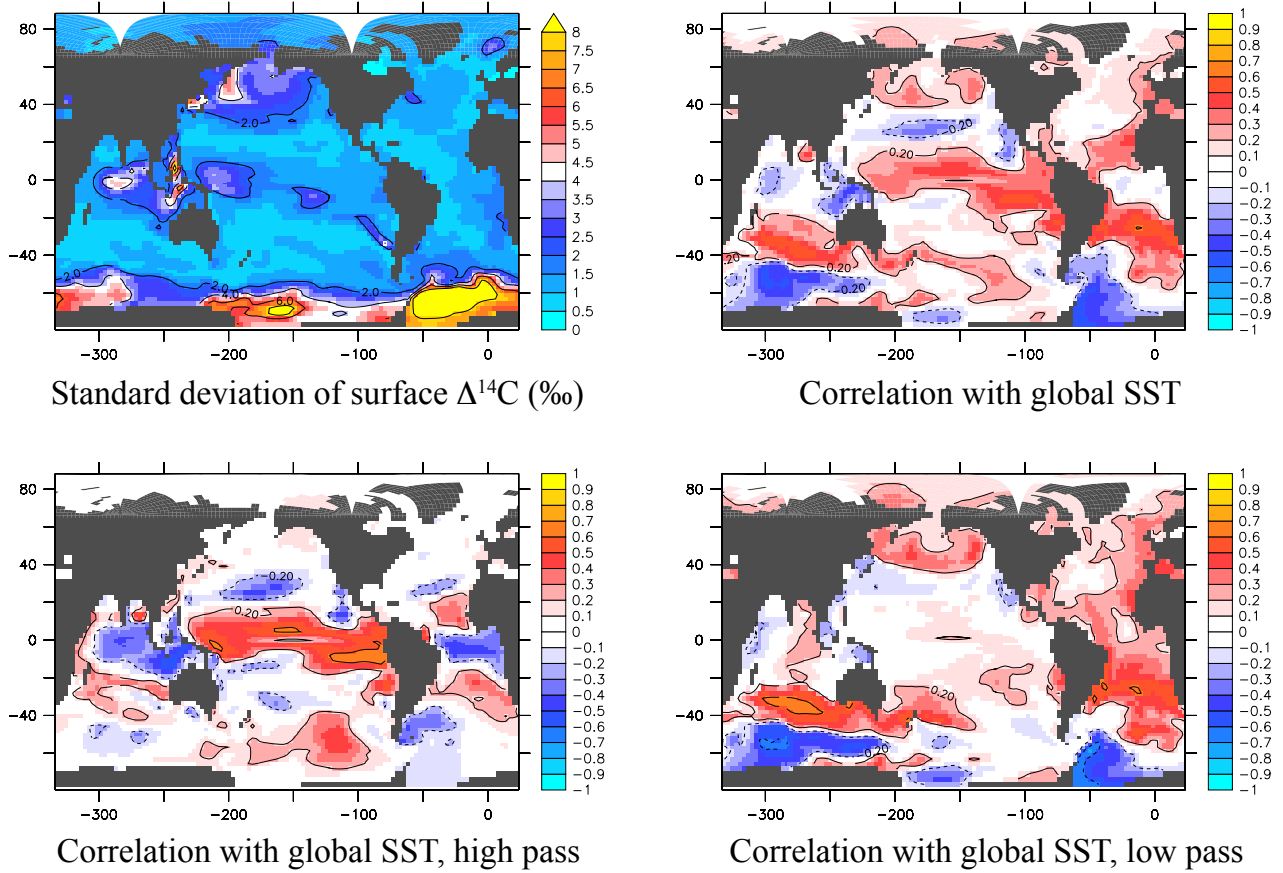


FIG. 7: Unforced variability in the simulation of temperature and $\Delta^{14}\text{C}$ at the sea surface. Top left, standard deviation of monthly-averaged $\Delta^{14}\text{C}$. Top right, correlation between surface $\Delta^{14}\text{C}$ and the globally averaged SST. Lower row, correlations between $\Delta^{14}\text{C}$ and both high-and low-pass filtered global SST (cutoff frequency 20y). All panels use monthly-averaged values of SST and/or $\Delta^{14}\text{C}$ over a continuous 500-year time interval. Note that large deviations of $\Delta^{14}\text{C}$, correlated with global temperatures, are found in both the vicinity of Indonesia and the high latitude Southern Ocean.

FIGURE 8

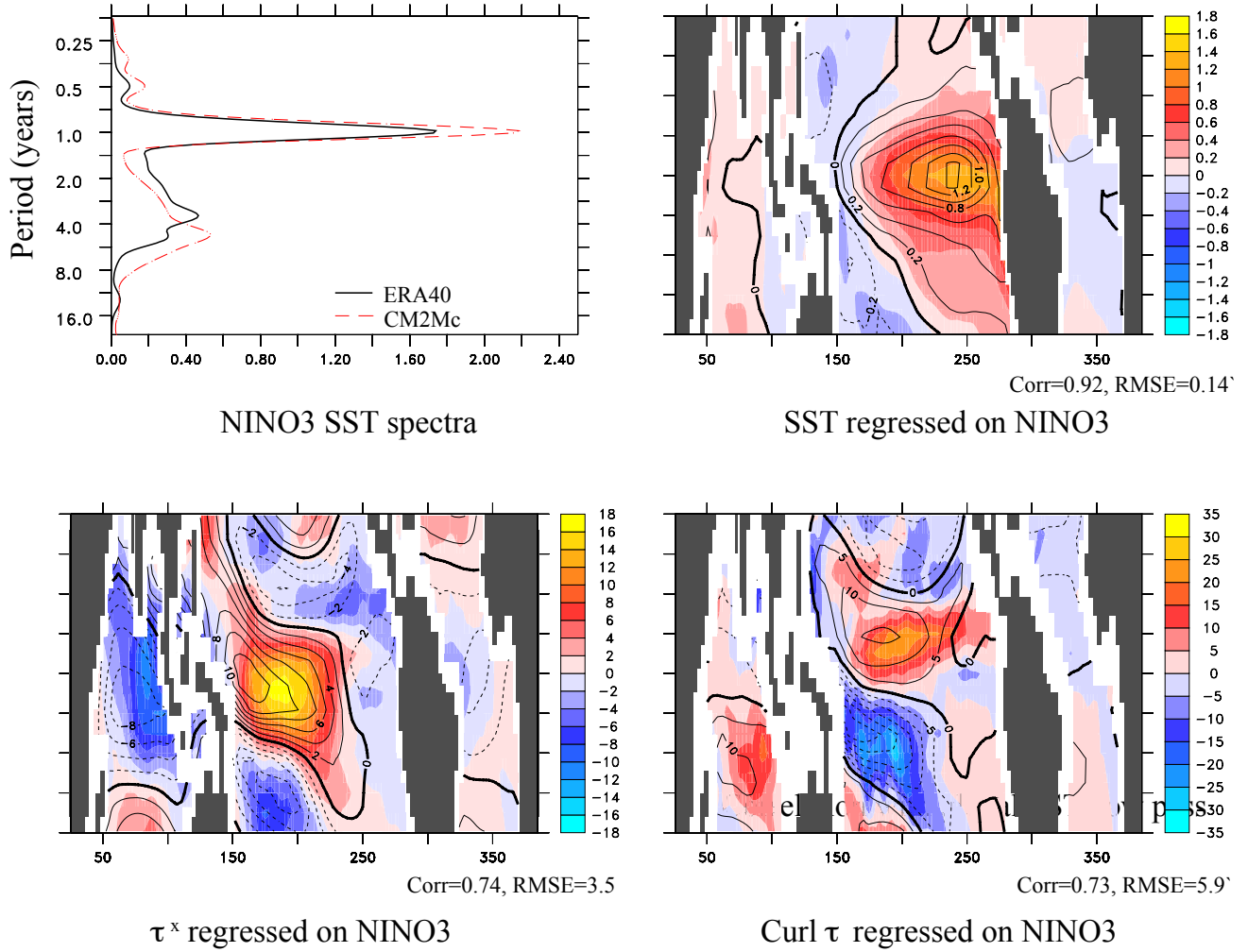


FIG. 8: Simulation of unforced ENSO-like variability. Top left, frequency spectrum of SST in the NINO3 region, observations (ERA40 reanalysis, black) and CM2Mc (red, dashed). Top right, regression of SST on NINO3 SST, observations (ERA40 reanalysis, colours) and CM2Mc (contours). Bottom left, as in top right, showing zonal wind stress on the ocean (N m^{-2}). Bottom right, as in top right, showing wind stress curl.

FIGURE 9

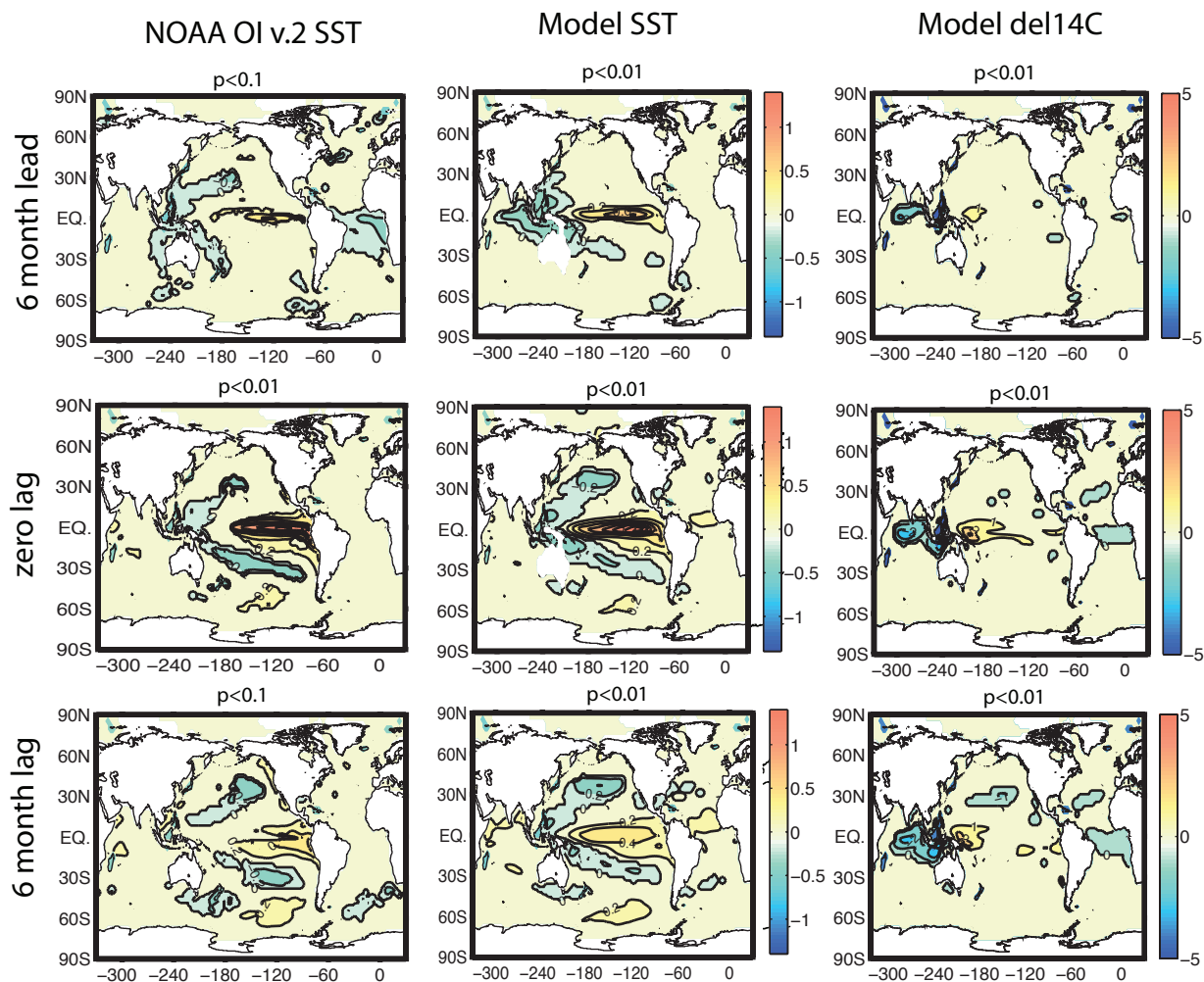


FIG. 9: Phasing between NINO3 SST and temperature or $\Delta 14C$ at the sea surface. The top row shows 6-month lead correlations between the indicated variable and NINO3 SST, the center row shows in phase correlations, and the bottom row shows 6-month lag correlations. The left column shows the regressions of observed SST (Reynolds et al., 2002), the center column shows the corresponding regressions for model SST, and the right column shows the regressions for model $\Delta 14C$.

FIGURE 10

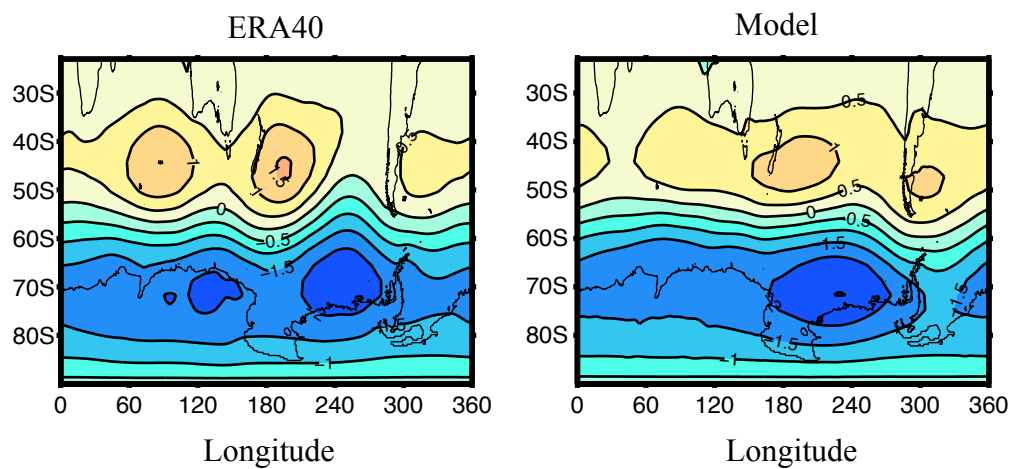


FIG. 10: Model simulation of SAM-like variability. The first Empirical Orthogonal Function (EOF) of the monthly sea level pressure anomaly south of 20°S is shown, as obtained from observations (ERA40, left) and model (right).

FIGURE 11

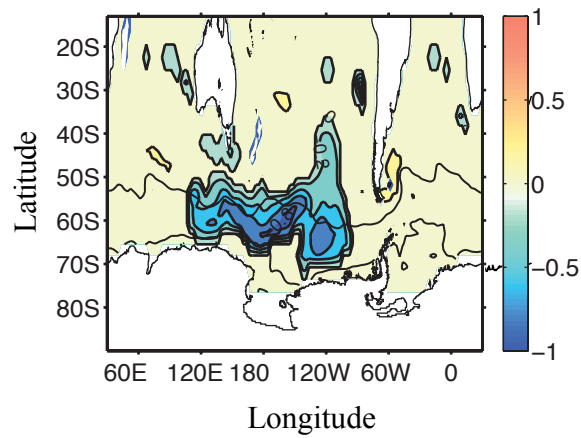


FIG. 11: Regression of simulated sea surface $\Delta^{14}\text{C}$ on SAM index. The annual mean SSH contours of -0.4 m (north) and -1.2 m (south) are superimposed in black solid lines to indicate the ACC after Dong et al. (2008). Although there is a negative correlation between surface $\Delta^{14}\text{C}$ and the SAM in the Pacific sector of the Southern Ocean, it explains only a very small amount of the variance, which is due instead to episodic convection.

FIGURE 12

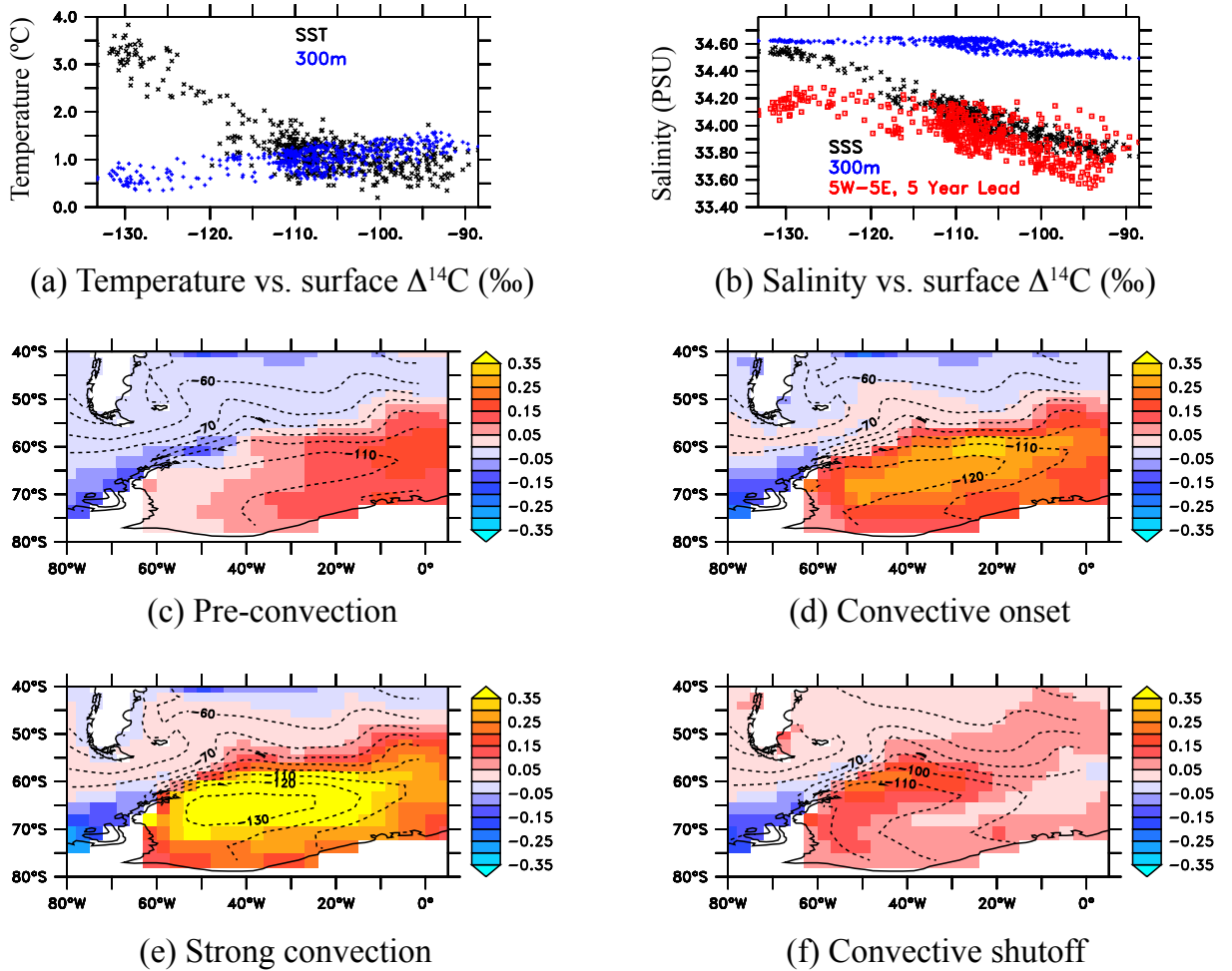


FIG. 12: Episodic convection events in the Weddell Sea. (a) Water temperature at two depths vs. surface $\Delta^{14}\text{C}$, averaged annually over 50°-30°W, 70°-60°S. When convection is active, the surface $\Delta^{14}\text{C}$ is low (left side of panel) and the surface is relatively warm, but the water at 300m is relatively cool. (b) As in (a), but showing salt instead of temperature. Panels (c) through (f) show the progression of salinity anomalies (colour) in association with ventilation events, as identified by the rate of change of water age on a 300m depth surface between 50°W-30°W and 70°S-60°S. Dashed contours show surface $\Delta^{14}\text{C}$, in permil.

FIGURE 13

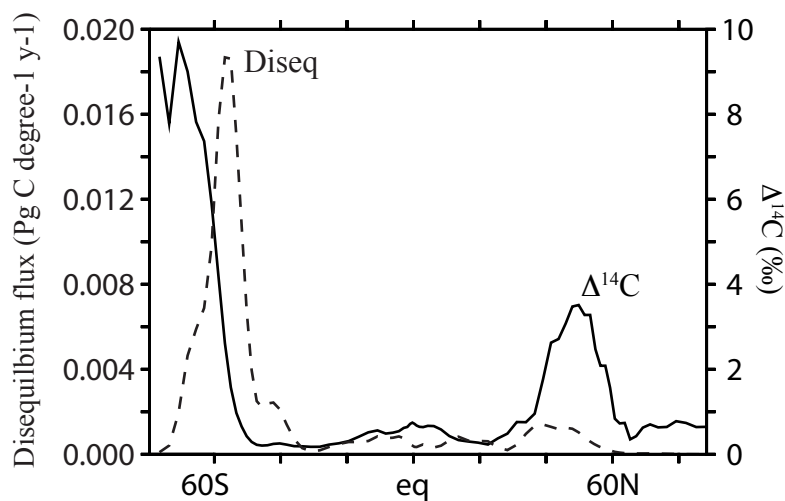


FIG. 13: Interannual variability in the air-sea radiocarbon fluxes. The interannual variability of surface $\Delta^{14}\text{C}$ (1 s.d.), zonally averaged, is shown by the solid line (right axis). The interannual variability of the disequilibrium flux (1 s.d.), zonally integrated, is shown by the dashed line (left axis).

FIGURE 14

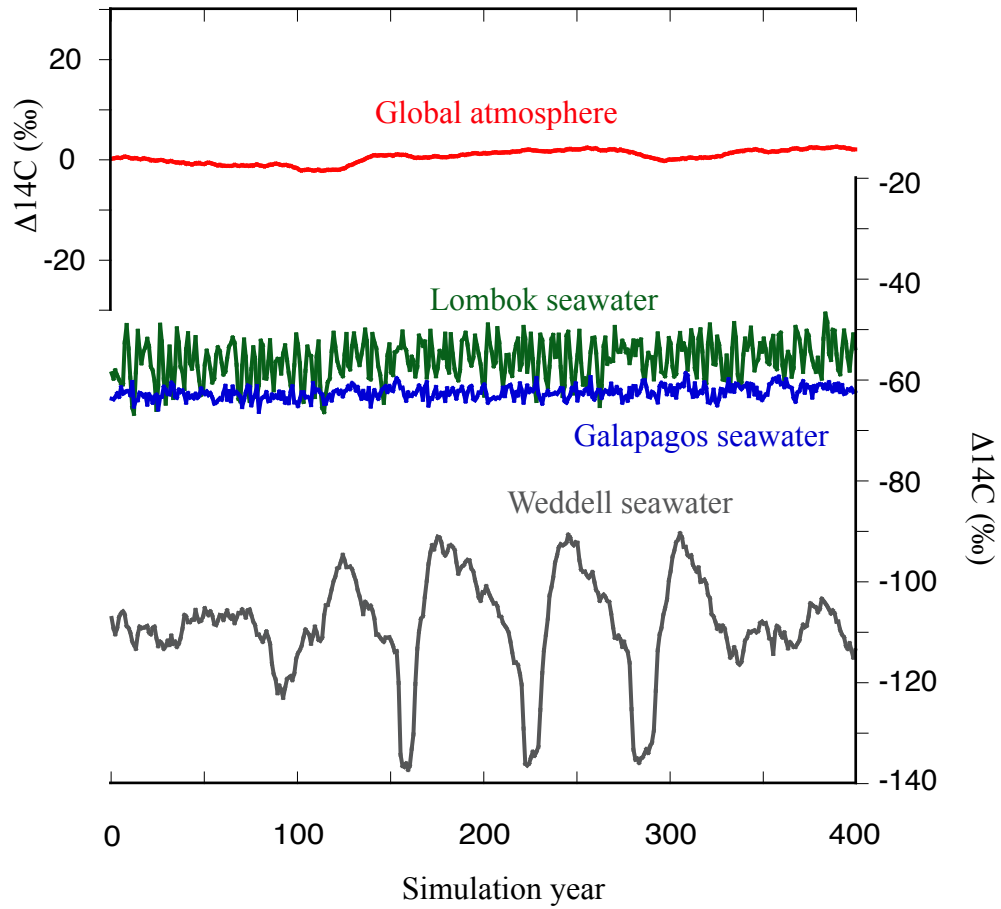


FIG. 14: Simulated atmospheric and seawater $\Delta^{14}\text{C}$ arising from unforced model variability over 400 years. The upper curve (red) approximates the variations in atmospheric $\Delta^{14}\text{C}$ expected from the simulated air-sea disequilibrium flux, as described in the text. The lower curves show the simulated variations in sea surface $\Delta^{14}\text{C}$ in the model (blue, Galapagos; green, eastern Indian Ocean, near the Lombok Strait; grey, central Weddell Sea). The axes are scaled to be approximately equivalent to the corresponding data shown in Figure 1.